

AD-A127 842

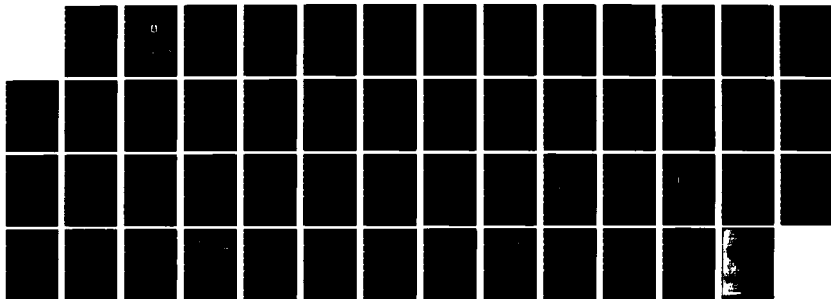
JOURNAL OF CHINESE SOCIETY OF ASTRONAUTICS (SELECTED
ARTICLES)(U) FOREIGN TECHNOLOGY DIV WRIGHT-PATTERSON
AFB OH Q C ZHOU 10 MAR 83 FTD-ID(R5)T-0084-83

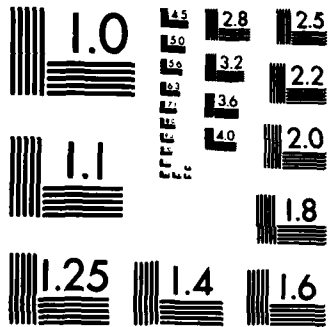
1/1

UNCLASSIFIED

F/G 22/1

NL





MICROCOPY RESOLUTION TEST CHART
NATIONAL BUREAU OF STANDARDS-1963-A

ADA 127842

FOREIGN TECHNOLOGY DIVISION



JOURNAL OF CHINESE SOCIETY OF ASTRONAUTICS

(Selected Articles)



DTIC
SELECTED
MAY 10 1983

A

Approved for public release;
distribution unlimited.

DTIC FILE COPY



83 05 09-038

EDITED TRANSLATION

FTD-ID(RS)T-0084-83

10 March 1983

MICROFICHE NR: FTD-83-C-000326

JOURNAL OF CHINESE SOCIETY OF ASTRONAUTICS
(Selected Articles)

English pages: 47

Source: Yuhang Xuebao, Nr. 3, 1982, pp. 57-89

Country of origin: China

Translated by: SCITRAN

F33657-81-D-0263

Requester: FTD/TQTA

Approved for public release; distribution unlimited.

THIS TRANSLATION IS A RENDITION OF THE ORIGINAL FOREIGN TEXT WITHOUT ANY ANALYTICAL OR EDITORIAL COMMENT. STATEMENTS OR THEORIES ADVOCATED OR IMPLIED ARE THOSE OF THE SOURCE AND DO NOT NECESSARILY REFLECT THE POSITION OR OPINION OF THE FOREIGN TECHNOLOGY DIVISION.

PREPARED BY:

TRANSLATION DIVISION
FOREIGN TECHNOLOGY DIVISION
WP-AFB, OHIO.

GRAPHICS DISCLAIMER

All figures, graphics, tables, equations, etc. merged into this translation were extracted from the best quality copy available.

CALCULATION OF MINIMUM ENTRY HEAT TRANSFER SHAPE OF A SPACE VEHICLE

Zhou Qi cheng

ABSTRACT

This paper dealt with the study of the minimum total heat transfer aerodynamic shape problem for a re-entry spacecraft. In this paper, the well known boundary layer heat transfer relation was used first to derive the expressions of the total heat flow rate on the surface of the spacecraft and the total heat added during the entire re-entry process. Then, with the aid of some numerical results, the flow field and the Prandtl-Meyer expansion theory, the minimum re-entry heat transfer shape under specified fineness ratio and total vehicle weight conditions could be obtained using a variational method. Finally, the effect of the drag coefficient on the minimum re-entry heat transfer shape was analyzed. The calculated results indicated that: For a given total vehicle weight and specified fineness ratio, the total heat transfer decreased with increasing drag coefficient. The minimum re-entry heat transfer shape is a cylinder with a flat nose.

I. INTRODUCTION

The rational section of the aerodynamic shape of the re-entry vehicle to reduce the heating due to surface convection to the maximum extent possible is very meaningful to the design of either retrievable satellites or missile warheads. It not only can effectively reduce the weight of the re-entry heat protection layer to improve the effective payload of the vehicle, but also is helpful in improving the accuracy of the calculation of the aerodynamic coefficients to improve the target hitting rate. Therefore, in recent years, many

This paper was received Sept. 24, 1981

researchers and engineering technical personnel are concerned about this problem. This paper involved the study of the minimum heat transfer aerodynamic shape problem of a re-entry vehicle on the basis of the design of a retrievable satellite. In order to simplify the problem, we assumed that during the re-entry flight process the geometrical shape of the vehicle remained unchanged. The geometrical slope of the surface of the object is greater or equal to zero.

References [1,2] studied the minimum heat flow rate shape with a specified fineness ratio when the flight Mach number remained unchanged under the assumption of Newtonian pressure. Reference [3] extended the problem to the entire re-entry flight and discovered that for a given trajectory coefficient ($\frac{M}{C_{DA}}$) and a specified fineness ratio, the minimum heat transfer shape is the minimum heat flow rate shape. Reference [4] applied the numerical values of inviscid flow to the problem discussed in [3]. The accuracy of the calculation of the minimum heat transfer shape was greatly improved. The minimum heat transfer shape (which is also the minimum heat flow rate shape) under laminar and turbulent flow conditions for a given trajectory coefficient obtained in that paper was a rotating body with a flat nose. The angles of inclination at the tip and the surface were about 20° and 17° , respectively. In [5], the actual requirement of an effective volume in the vehicle was taken into account during the engineering design. Therefore, the work carried out in [3,4] was further extended. The minimum heat transfer shape of a re-entry flight vehicle in laminar and turbulent flow condition with a given trajectory coefficient, a specified fineness ratio and a specified effective volume was calculated. Furthermore, the analytical expression of the minimum heat transfer shape under laminar flow condition with a specified trajectory coefficient and a specified effective volume (no requirement was needed for the fineness ratio) was obtained. The above references did not involve the effect of the variation of drag coefficient on the minimum heat transfer shape.

In the actual engineering design, people frequently wanted to know the shape of the minimum re-entry heat transfer under a given total weight and a specified fineness ratio. Because the re-entry

trajectory coefficient is an important parameter influencing the re-entry flight, the variation of drag coefficient will directly vary the trajectory coefficient. Consequently, the total added heat to re-entry will be affected. Therefore, in the optimization of the aerodynamic shape, it is necessary to analyze the effect of the drag coefficient of the re-entry body on the re-entry heat. The study of whether the minimum heat flow rate shape is still the minimum re-entry heat transfer shape is very important. The purpose of this paper is to find the minimum re-entry heat transfer shape with specified fineness ratio and total vehicle weight.

II. PRESENTATION OF THE PROBLEM

The commonly adopted LEES laminar flow heat transfer theory [6] and VAGLIO-LAURIN turbulent flow heat transfer theory [7] are used to calculate the surface heat flow rate of the re-entry vehicle

$$q = \frac{C_N \rho_e V_w H_e}{(\rho_e V_w R_B / \mu_e)^{1/n}} \cdot \frac{\bar{\rho}_e \bar{u}_e \bar{\mu}_e y^{\frac{1}{n-1}}}{\left[\int_0^y \bar{\rho}_e \bar{u}_e \bar{\mu}_e y^{\frac{n}{n-1}} ds \right]^{1/n}}$$

where

$$C_N = \begin{cases} 0.0332 P_r^{-1/2} g (1 - H_w / H_e) & \text{laminar flow} \\ 0.0296 P_r^{-1/2} g (1 - H_w / H_e) & \text{turbulent flow} \end{cases}$$

ρ , u , μ and H represent the density, tangential velocity, viscosity coefficient and enthalpy of the flow, respectively
 $(\bar{\rho}_e = \rho_e / \rho_o, \bar{u}_e = u_e / \sqrt{2H_e}, \bar{\mu}_e = \mu_e / \mu_o)$, y and s represent the dimensionless abscissa of the vehicle shape and the arc length along the surface, respectively ($y = Y/R_B, s = S/R_B$), where R_B is the radius of the base. P_r is the Prandtl number and g is the gravitational acceleration. The subscripts e , o and w represent the values at the outer fringe, stationary point, and the wall of the boundary layer, respectively. $n = 2$ represents laminar flow and $n = 5$ represents turbulent flow. By introducing the following symbol

$$\varphi = \bar{\rho}_e \bar{u}_e \bar{\mu}_e y^{\frac{n}{n-1}}$$

and integrating the heat flow rate along the surface of the flight vehicle, we can obtain the total heat flow rate on the surface of the flight vehicle as

$$Q = \frac{2\pi R_s^{\frac{n}{n-1}} C_H \rho_0 V_\infty H_s}{(\rho_0 V_\infty R_s / \mu_0)^{1/n}} \left[\int_0^s \phi ds \right]^{\frac{n-1}{n}}$$

It is commonly known that the stationary point heat flow rate is related to the radius of curvature of the object at the stationary point. The magnitude of the heat flow rate increases or decreases with increasing or decreasing radius of curvature. Therefore, it is reasonable to believe that the minimum heat transfer shape is composed of a flat nose and a rear body part [1,4]. Hence, by using the isoenthalpy relation and the viscosity exponent law, we can express the integral in the above equation as

$$I = \int_0^s \phi ds = \psi_1(M_\infty) \left[I_1 + \int_{y_1}^s F(P, z, y) dy \right]$$

where

$$F(P, z, y) = P^a (1 - P^b)^{a+b} (1 + z^2)^{a+b} y^{\frac{n}{n-1}}$$

$$\psi_1(M_\infty) = \left[\frac{2}{(\gamma - 1) M_\infty^2} + 1 \right]^{a+b}$$

$$a = \frac{1 + (\gamma - 1)\omega}{\gamma}$$

$$b = \frac{\gamma - 1}{\gamma}$$

γ is the specific heat of air, ω is the viscosity exponent, y_1 is the height of the flat nose, M_∞ is the flight Mach number and P is the pressure coefficient which is defined as $P = \frac{P_s}{P_\infty}$, $z = \frac{dx}{dy}$, x is the dimensionless ordinate of the flight vehicle shape $x = \frac{X}{R_s}$, and I_1 is the integral on the flat nose.

$$I_1 = \int_0^{y_1} P^a (1 - P^b)^{a+b} y^{\frac{n}{n-1}} dy$$

If we assume that the sonic point is located at the intersection of the flat nose and the rear body, then it is possible to complete this integration by using the simplified integral relation [8] or an inviscid flow numerical value. Therefore, it is a known constant. We can rewrite it as

$$I_1 = \left(\frac{\gamma - 1}{\gamma + 1} \right)^{a+b} J_s y_1^{1 + \frac{n}{n-1}}$$

where J_s is a known constant and its value differs for laminar flow and turbulent flow.

Based on the differential correlation between the total heat flow rate \dot{Q} and the total re-entry heat Q

$$\dot{Q} = \int \dot{Q} dt = - \int_{h_E}^{h} \dot{Q} \frac{dt}{dh} dh$$

and the CHAPMAN [9] trajectory approximation which is applicable to trajectories with larger variation of the angle of inclination θ

$$\frac{dh}{dt} = V_{\infty} \cdot \sin \theta$$

we can express the total re-entry flight heat as

$$Q = -2\pi R_E^2 \frac{\rho_0}{n-1} \int_{h_E}^{h} \frac{C_H \rho_0 H_0}{(\rho_0 V_{\infty} R_E / \mu_0)^{1/n} \cdot \sin \theta} \left[\int_0^{\phi} \phi ds \right]^{\frac{n-1}{n}} dh$$

where V_{∞} is the flight speed, h is the flight altitude, t is the flight time and h_E is the upper fringe height of the dense atmosphere.

For an Earth orbit re-entry flight vehicle, aerodynamic heating primarily occurs during the hypersonic flight stage ($M_{\infty} \gg 1$). In an approximation analysis, it can be considered that the pressure coefficient of the rear body is not related to the Mach number of the incoming flow (such as the Newtonian theory or the P-M expansion theory). It is only a function of the geometric position. Therefore, the integration with respect to ϕ in the above formula can be extracted from the integration with respect to h . Hence, it is possible to use the relationship before and after the normal shock wave, the isoenthalpic correlation and the CHAPMAN approximation trajectory to finally simplify the total re-entry heat formula under the condition that $M_{\infty} \gg 1$ as

$$Q = A_{\infty} B \left[\frac{I}{C_D A / M} \right]^{1 - \frac{1}{n}} \quad (1)$$

where

$$B = \int_0^{\phi_{max}} \frac{U^{1 + \frac{2\sigma}{n}} \phi(M_{\infty})}{Z^{\frac{1}{n}} (\cos \theta)^{2 - \frac{1}{n} + \frac{2\sigma}{n}}} dU$$

$$\theta = \sin^{-1} \left[\left(\frac{dZ}{dU} - \frac{Z}{U} \right) / \sqrt{R\beta} \right]$$

$$\phi(M_{\infty}) = \phi_1(M_{\infty}) \cdot \frac{\left(\frac{\gamma+1}{2} M_{\infty}^2 \right)^{\frac{\gamma}{\gamma-1}}}{\left(1 + \frac{\gamma-1}{2} M_{\infty}^2 \right) \left(\frac{2\gamma}{\gamma+1} M_{\infty}^2 - \frac{\gamma-1}{\gamma+1} \right)^{\frac{1}{\gamma-1}}}$$

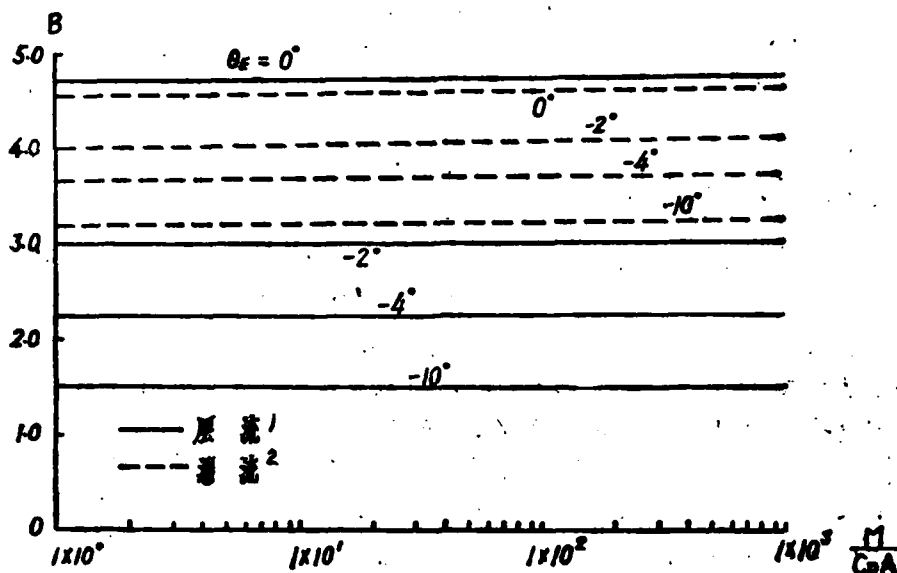


Figure 1. The variation of B with the re-entry angle and the trajectory coefficient
1--laminar flow; 2--turbulent flow

β is the reciprocal of the density of the atmosphere, and R is the average radius of the Earth. From [9], we know that the dimensionless CHAPMAN variables Z and dZ/dU are known functions of the dimensionless velocity U which is only related to the re-entry angle θ_E . The functional relationship between M_∞ and U is only related to $M/C_D A$. Actual computation showed that B is a function of the re-entry angle. The effect of the trajectory coefficient can be completely neglected. The details are shown in Figure 1. A is the reference area of the drag coefficient C_D , M is the mass of the flight vehicle and A_m is a constant. Its expression is

$$A_m = \frac{n}{n-1} 2^{1-\frac{1}{n}} C_D \pi R_E^2 \left(\beta R \right)^{\frac{n-1}{n}} g^{1-\frac{1}{2n}+\frac{\sigma}{n}}$$

$$\times \beta^{-\frac{n+1}{2n}} R^{\frac{1}{2}+\frac{\sigma}{n}} \mu_E^{\frac{1}{n}} V_E^{-\frac{2\sigma}{n}}$$

where V_E and μ_E are the re-entry velocity and the air viscosity coefficient at the initial re-entry altitude.

The so-called minimum heat transfer shape is the geometric shape with which the total re-entry heat Q of the flight vehicle surface is the minimum. If $x = x(y)$ is used to represent the equation of the

parent line of the minimum heat transfer shape, it can be substituted into the computational expression of Q derived above as equation (1) and Q will have the minimum value. Therefore, solving for the minimum heat transfer shape under specified fineness ratio and total vehicle weight can be mathematically reduced to the solving of the minimum curve of the generalized function I/C_D inside the bracket in (1). That is to find the minimum curve of the following mixed type generalized function with moving boundary points.

$$I^*[x(y)] = \frac{\left(\frac{y-1}{y+1}\right)^{n+1} J_{K y_1}^{1 + \frac{n}{n-1}} + \int_{y_1}^1 F(P, x, y) dy}{C_D} \quad (2)$$

where

$$C_D = 4 \int_0^{y_1} P y dy + 4 \int_{y_1}^1 P y dx$$

The first term of the formula represents the contribution of the flat nose to the drag. It is possible to use the simplified integral relation [8] to complete this integration. Or, it is also possible to compute it based on the results of the numerical values of an inviscid flow. The second term represents the contribution of the rear body to the drag. In order to facilitate the use in the future, we are rewriting the above formula as

$$C_D = 4 J_D y_1^2 + 4 \int_{y_1}^1 P y dy \quad (3)$$

where J_D is a known constant.

If τ is used to represent the fineness ratio ($\tau = 2R_n/L$), of the flight vehicle, then the boundary condition can be expressed as

$$x(1) = \frac{2}{\tau} \quad (4)$$

Because we did not specify the height of the flat nose y_1 , it is a quantity to be determined. In order to have a solution to the variational problem, we must supplement the so-called crossing condition to be satisfied by the minimum curve at $x = 0$. Its actual form is related to the treatment method of the problem.

Equations (2), (4) and the crossing condition at $x = 0$ are the original equations to solve for the minimum re-entry heat transfer

shape for a specified total vehicle weight and fineness ratio.

III. SOLUTION OF THE VARIATIONAL EQUATION

The minimum heat transfer shape for a given total vehicle weight M and specified fineness ratio τ can be found by solving the variational problem in equations (2) and (4) directly. However, in order to facilitate the analysis of the effect of the variation of drag coefficient C_D on the minimum heat transfer shape, we chose to use the following method. It involved the use of a series of properly chosen specified values of drag coefficients $C_{D,i}(i=1,2,3\dots)$. Then, the minimum heat transfer shapes and the total re-entry heats correspond to these specified values of drag coefficients. Therefore, we can understand the effect of drag coefficient on the minimum heat transfer shape and the total heat from this series of calculations. In the meantime, it is not difficult to find the eventually needed minimum heat transfer shape for a given total weight and a specified fineness ratio.

According to our knowledge in the variational method [10], the minimum re-entry heat transfer shape for a specified drag coefficient is reduced to the solution of the minimum curve for the following generalized function

$$I^{**}[x(y)] = \left(\frac{\gamma-1}{\gamma+1}\right)^{\frac{n}{2}} J_{K y_i}^{1 + \frac{n}{n-1}} - \lambda_1 C_D + 4\lambda_1 J_{D y_i} + \int_{y_1}^1 F^{**} dy \quad (5)$$

where λ_1 is the Lagrange coefficient yet to be determined

$$F^{**} = F + 4\lambda_1 P y$$

The boundary condition is the same as before as shown in equation (4).

The crossing condition is

$$J_K \left(\frac{\gamma-1}{\gamma+1}\right)^{\frac{n}{2}} \left(1 + \frac{1}{n-1}\right) y_i^{\frac{n}{n-1}} + 8\lambda_1 J_{D y_i} - \left(F^{**} - z \frac{dF^{**}}{dz}\right)_{y=y_1} = 0 \quad (6)$$

In order to determine the Lagrange coefficient λ_1 , it is necessary to simultaneously solve for the constraint equation (3) in which the drag coefficient is equal to a specified value.

Up until the present moment, we only assumed that the junction

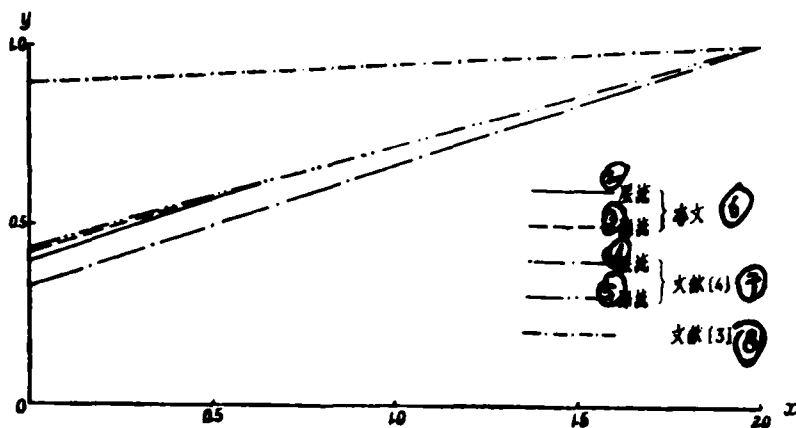


Figure 2. The minimum heat transfer shape for a given trajectory coefficient ($\tau = 1.0$)
 2--laminar flow; 3--turbulent flow; 4--laminar flow; 5--turbulent flow; 6--this paper; 7--reference [4]; 8--reference [3]

between the flat nose and the rear body is a sonic point and its pressure coefficient is not related to the Mach number of the incoming flow. References [1-3] used the Newtonian theory to calculate the pressure distribution on the rear body. However, the minimum heat transfer shape they obtained is quite different from the one obtained in [4] using the inviscid flow numerical solution as a basis. By taking into account that fact that the variational method requires that the rear body pressure distribution starting from the sonic point must be continuous and differentiable, we used the P-M expansion theory to calculate the rear body pressure distribution in this paper. Although by doing so it is possible that the numerical value of the rear body pressure coefficient might be underestimated, yet in actual trial computation, it was discovered that the major factors affecting the minimum heat transfer shape are the pressure distribution on the flat nose and the pressure variation near the junction between the flat nose and the rear body. By using the P-M expansion theory, the pressure variation near the junction can be better reflected. From Figure 2, we can see that the minimum heat transfer shape for a given trajectory coefficient using the P-M expansion theory in this paper agrees with that obtained based on the inviscid flow numerical solution in [4] comparatively well. As can be expected, when the calculated results converged to approach the minimum curve (later, we will see that the minimum heat transfer shape is a cylinder with a flat

nose), the accuracy of the rear body pressure distribution calculated using the P-M expansion method is improved. In addition, we should also point out that the treatment in this paper is focused on the study of the variation trend of the target function (i.e., the total re-entry heat) rather than the numerical value of the target function itself. The computational error of the rear body pressure distribution will not cause the variation of the trend of the variation of the total re-entry heat. Therefore, it is believed in this paper that it is feasible to use the P-M expansion theory to calculate the rear body pressure distribution as an approximate analysis.

When we use the P-M method to calculate the pressure on a conical body, the pressure coefficient is only related to the local slope dx/dy . According to our knowledge in the variational method, the Euler equation of this type of variational problem has a simple integral:

$$\frac{\partial F}{\partial z} + 4\lambda_1 y \frac{\partial p}{\partial z} = C$$

where C is an integration constant yet to be determined by the boundary condition. The above equation can be integrated once more into the following form:

$$\left\{ \begin{aligned} x = \int_{z_1}^{z_2} z \frac{4\lambda_1 \frac{\partial^2 p}{\partial z^2} - y^{\frac{n}{n-1}} f'(z)}{\frac{n}{n-1} f(z) y^{\frac{n}{n-1}} - 4\lambda_1 \frac{\partial p}{\partial z}} dz & \quad (7) \\ y^{\frac{n}{n-1}} \cdot f(z) - 4\lambda_1 \frac{\partial p}{\partial z} = -C & \end{aligned} \right.$$

where

$$f(z) = -y^{-\frac{n}{n-1}} \frac{\partial F}{\partial z}, \quad f'(z) = -y^{-\frac{n}{n-1}} \frac{\partial^2 F}{\partial z^2}$$

z_1 and z_2 are the slopes of the minimum curve at $x = 0$ and $x = 2/\tau$ respectively. They are both unknown quantities.

Substituting the correlations of the P-M expansion theory

$$P = \left(1 - \frac{\gamma-1}{\gamma+1} \lambda_1^2\right)^{\frac{\gamma}{\gamma-1}}$$

$$\alpha \sin^{-1}\left(\frac{1}{\lambda}\right) = \sqrt{\frac{\gamma+1}{\gamma-1}} \sin^{-1}\left(\sqrt{\frac{(\gamma-1)(\lambda^2-1)}{2}}\right) - \sin^{-1}\left(\sqrt{\frac{(\gamma+1)(\lambda^2-1)}{2}}\right)$$

into the above equation, it is possible to find the actual computational expressions for $f, f', \frac{\partial p}{\partial x}$ and $\frac{\partial^2 p}{\partial x^2}$ through not too complicated derivations. Therefore, by simultaneously solving for equations (3), (4), (6) and (7), we can obtain the minimum re-entry heat transfer shape for a drag coefficient equal to a specific value.

IV. COMPUTATIONAL RESULTS AND DISCUSSION

We computed the minimum re-entry heat transfer shapes for various fineness ratios with drag coefficients as a series of specific values under the conditions that $\gamma=1.2, \omega=1.0$, and $dy/dx \geq 0$. The numerical values of J_K and J_D were obtained from the results in [4]. In the following, we will briefly introduce the calculated results.

Figure 3 plots out the minimum re-entry heat transfer shapes with drag coefficients equal to a series of specific values. C_{D0} is the drag coefficient of the minimum heat flow rate shape (i.e., the minimum heat transfer shape studied in [4]). From this figure, we can see that the minimum re-entry heat transfer shape is a family of flat headed rotating bodies. With increasing drag coefficient, the height of the flat nose is gradually higher and the half vertex angle of the rear body is becoming smaller. The rear body more and more approaches a cone. The laminar flow minimum re-entry heat transfer shape and the turbulent flow minimum re-entry heat transfer shape are very close.

Figure 4 plots the minimum re-entry heat transfer shape total heat flow rate for various drag coefficient equal to different specific values. \dot{Q}_0 is the minimum heat transfer shape total heat flow rate under invariant trajectory coefficient conditions. From the figure, we can see that when the drag coefficient is not equal to C_{D0} , the total heat flow rate \dot{Q} is always higher than \dot{Q}_0 . It is true for both laminar flow and turbulent flow. The reason is very simple.

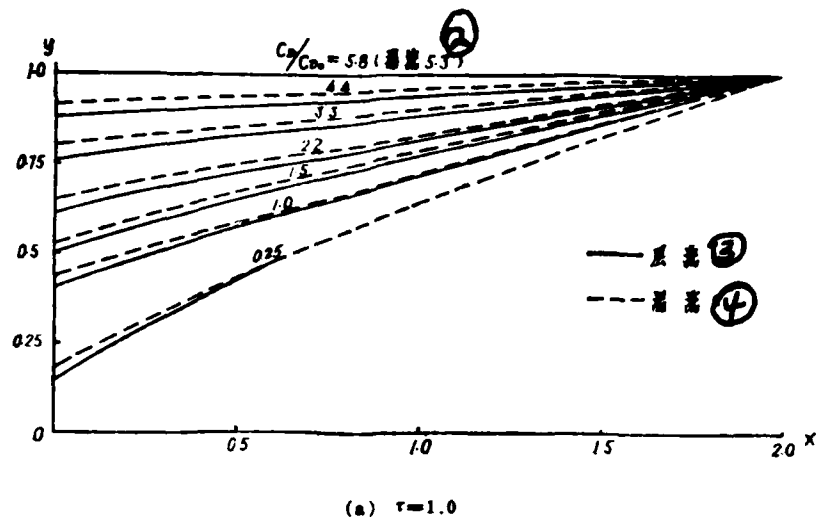


Figure 3. The minimum re-entry heat transfer shape when the given drag coefficient is a fixed value
 2--turbulence; 3--laminar flow; 4--turbulent flow

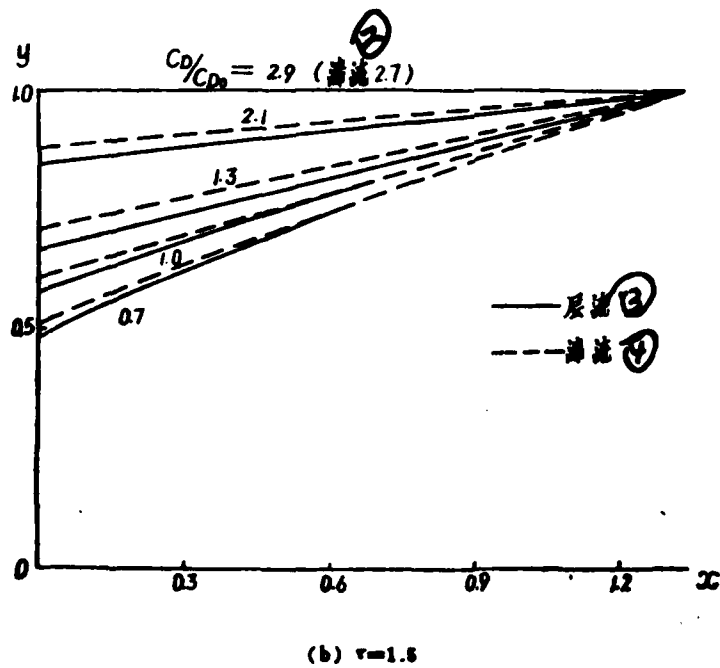


Figure 3. (continuation)
 2--turbulent flow; 3--laminar flow; 4--turbulent flow

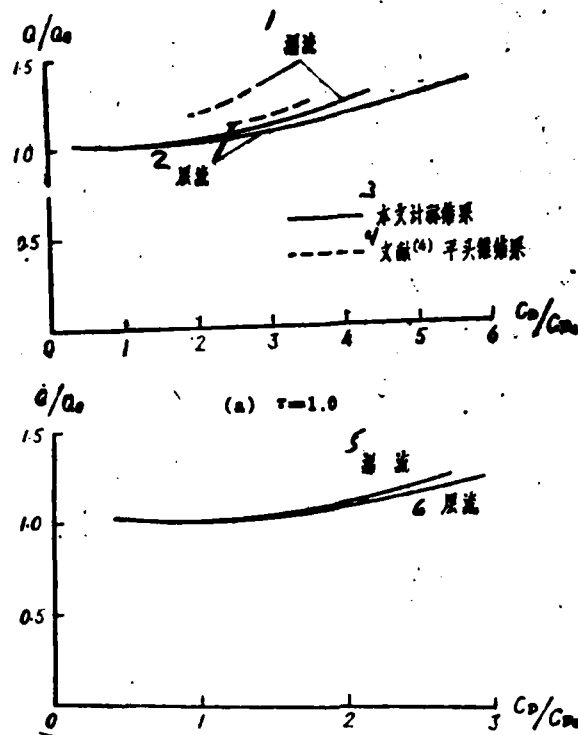


Figure 4. The variation of the minimum heat transfer shape total heat flow with drag coefficient when the drag coefficient is a fixed value
 1--turbulent flow; 2--laminar flow; 3--calculated results in the paper; 4--flat heated cone results from [4]; 5--turbulent flow; 6--laminar flow

It has been pointed out in [4,5] that when the trajectory coefficient is unchanged, the minimum re-entry heat transfer shape is the minimum heat flow rate shape. Therefore, when C_D is different from C_{D0} , the \dot{Q} is naturally higher than \dot{Q}_0 .

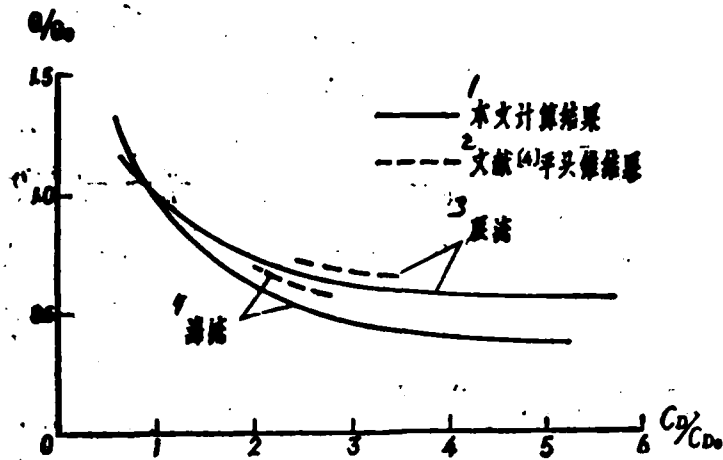
Figure 5 plots the minimum re-entry heat transfer shape total heat corresponding to various drag coefficients which are equal to different specific values. The reference values used in the figure are similar to those in Figure 4. From this figure, we can clearly see that the re-entry total heat rapidly decreases with increasing drag coefficient. When the drag coefficient C_D increased to the value equal to that of a flat nosed cylinder, the re-entry total heat

reached the minimum. This variation trend indicates that, although the increase in drag coefficient would cause the surface total heat flow rate to increase, yet, under a given total re-entry weight condition, the increase in drag coefficient would simultaneously cause the trajectory coefficient to drop rapidly. The net effect is to gradually reduce the total heat. From Figure 5, it is not difficult to see that when the re-entry weight is specified, the minimum re-entry heat transfer shape is a flat headed cylinder.

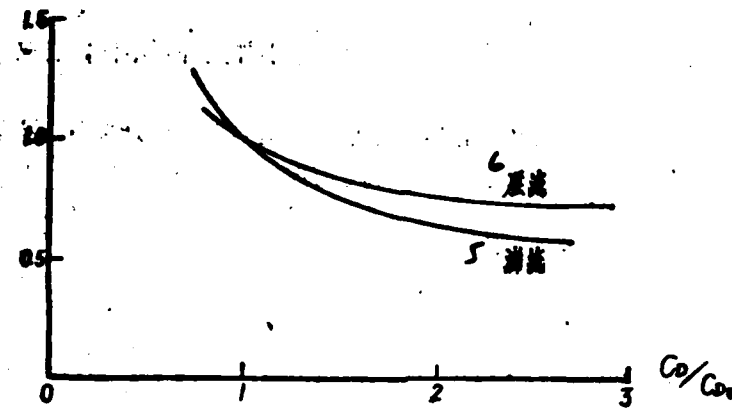
Figures 4 and 5 also plotted the calculated results of the flat headed cone part using the inviscid flow numerical solution as the basis. The variation trend agrees with the calculated results in this paper. When the drag coefficient is identical, the total heat flow rate and the total heat of the flat headed cone are higher than the calculated results of the minimum re-entry heat transfer shape in this paper.

Figure 6 plots the calculated results of a flattened cone and a spherical cone which are very close to the minimum heat transfer shape [4]. From the figure, we can see that the drag coefficient of a flat headed cone is higher than that of a spherical cone with the same half conical angle. When their half conical angles are identical, although their total heat flow rates (i.e., I) are not too different, yet the re-entry total heat of the flat nosed cone (i.e., I/C_D) is much lower than that of the spherical cone. In addition, we can also see from Figure 6 that in the half conical angle range shown, regardless of the spherical cone or the flat headed cone, the surface total heat flow rate gradually increases with increasing drag coefficient (i.e., the re-entry body becomes dull). The re-entry total heat gradually decreases.

According to the calculated results shown in Figures 4, 5 and 6 we seem to be able to draw the following conclusions: for a specified total re-entry weight, during the selection of the shape of the re-entry vehicle, we should choose a flat headed rotating body on the basis of satisfying other objectives of the whole body in order to

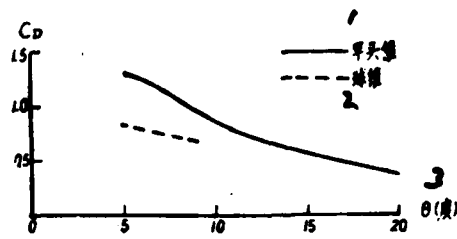


(a) $\tau=1.0$



(b) $\tau=1.5$

Figure 5. The variation of minimum heat transfer shape total heat with drag coefficient when the drag coefficient is a fixed value
 1--calculated results in this paper; 2--the flat headed cone results in [4]; 3--laminar flow; 4--turbulent flow; 5--turbulent flow; 6--laminar flow



(a) $C_D \sim \theta$

Figure 6. Comparison of heating of a flat headed cone to a spherical cone ($\tau = 1.0$)
 1--flat headed cone; 2--spherical cone; 3--degree

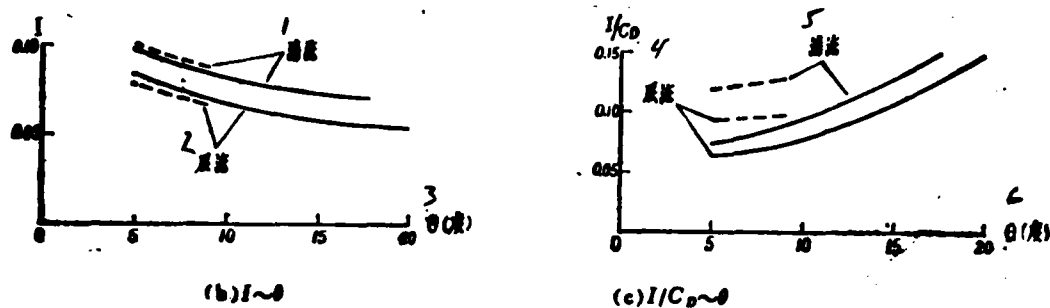


Figure 6 (continued)

1--turbulent flow; 2--laminar flow; 3--degree; 4--laminar flow; 5--turbulent flow; 6--degree

greatly reduce the re-entry heat to the maximum extent possible and to reduce the weight of the re-entry heat proof layer. Furthermore, we should attempt to use a larger drag coefficient to the extent possible. The flat headed cone is an aerodynamic shape with some future.

V. BRIEF CONCLUSIONS

1. The minimum re-entry heat transfer shape when the drag coefficient is equal to some specific number is a family of flat headed rotating bodies.

2. Along with increasing drag coefficient, the total heat flow rate of the flat headed rotating body is reduced monotonically. After reaching the minimum, it monotonically increases. The re-entry total heat monotonically decreases with increasing drag coefficient.

3. The minimum re-entry heat transfer shape for a given re-entry total weight is different from the minimum heat transfer shape for a given trajectory coefficient. It is a flat headed cylinder.

4. In order to reduce the re-entry heat to the maximum extent possible, while satisfying other functional objectives, we should

choose a flat head rotating body. Furthermore, a larger drag coefficient shape should be used to the extent possible. The flat headed cone is a promising aerodynamic shape.

REFERENCES

1. N.M. Velyanin. Izvestiya AN SSSR, MZhG, No. 6, 37, 1967.
2. V.D. Perminov, Ye.Ye. Solodkin. Izvestiya AN SSSR, MZhG, No.2,94,1971.
3. R.L. Baker and R.F. Kramer, AIAA Paper 77-780, 1978.
4. R.L. Baker and R.F. Kramer. AIAA Paper, 79, 0201, 1979.
- [5] Zhou Qicheng. "The minimum heat transfer aerodynamic shape of a re-entry flight vehicle", Chinese Space Science Technology, vol. 2, 1982.
- [6] LEE, L. JET PROPULSION, Vol. 26, No. 4, 1956.
- [7] VAGLIO-LAUREN, R. JOURNAL OF THE AERO/SPACE SCIENCE, Vol. 27, No. 1, 1960.
8. Chernyy, G.G. Doklady AN SSSR, Vol. 155, No. 2, 1964.
9. Dean. R. Chapman, NASA, TR-11, 1960.
- [10] L.E. Eleyaov. Variational Method, People's Education Publication translated Chinese edition, 1958.

ERRATA FOR VOL. 2, 1982, OF THIS JOURNAL

1	頁碼	2	誤	3	正
4	45頁第2行		$SX(\omega) = H(j\omega) \cdot SY(\omega)$		$SX(\omega) = H(j\omega) ^2 \cdot SY(\omega)$
5	47頁倒數第10行		$A_{n+1} = 3\sigma_1 + \sigma \quad (13)$		$A_{n+1} = 3\sigma_1 + \sigma \quad (12)$
6	60頁倒數第3行末		$-\dots + \xi \cdot \varphi(\xi) - \xi^2$		$-\xi + \varphi(\xi) - \xi^2 / \sigma^2$

1--page number; 2--wrong; 3--correct; 4--page 45 line 2;
 5--page 47, line 10 from the bottom; 6--page 60 end of line 3
 from the bottom

LIMIT ANALYSIS OF THE STRUCTURAL STRENGTH FOR THE COMBUSTION CHAMBER OF A LIQUID ROCKET ENGINE

ABSTRACT

This paper is an actual example of the limit analysis method in mechanics. It provided computational formulas for the limiting load of the major parts in the combustion chamber of a liquid rocket engine. These calculated results have good engineering accuracy in approximation through experimental verification.

I. INTRODUCTION

Due to the "short time" and "single use" characteristics of the liquid rocket engine, it is believed to be reasonable for part of its components to work in a plastic state or for the entire unit to approach the plastic state. To design a liquid rocket engine according to this viewpoint will enable us to fix the load resistance potential of the structure to the maximum degree possible. Consequently, the weight strength ratio of the engine can be rationally designed.

In the 60's, the workers in mechanics in our country conducted a lot of work in the areas of limit analysis and limit design to solve the common engineering shell limit analysis method. Furthermore, this method was developed to establish its theoretical basis to promote the flourishing development of this technology. This situation makes it not only necessary, but also possible to use the limit analysis method in a liquid rocket engine.

The limit analysis method is an important branch in plastic mechanics. Rigorously speaking, it is an engineering approximation method. Actual practice proved that the conclusions obtained by using this method had the sufficient engineering approximation. Because of the ease of use and the clear physical concept of this method, we

This paper was received on July 31, 1981.

believe that the application of limit analysis to the design of liquid rocket engine strength should have some constructive effect for a long time to come.

Finally, it should be pointed out that all the components of the liquid rocket engine are located in a strong vibration environment. Dynamic characteristic design and calibration are sometimes necessary for some components. This paper did not involve any discussion in this aspect.

II. THE LIMIT ANALYSIS OF THE LOADED TOP COVER OF THE COMBUSTION CHAMBER

The form of the loaded top cover is dependent on the supporting condition of the combustion chamber. It is also related to the required dimension of the entire unit. The usual forms are the spherical top cover, which is a part of the sphere. It is a more advantageous structural form to sustain a uniformly distributed pressure.

The triple centered top cover. By using such a structural form, it is not only possible to take care of the favorable form in maintaining the structure under high working pressure, but also able to take the requirement of reducing the total length dimension of the entire unit into account.

The conical top cover. When the thrust of the engine is transferred from the head of the combustion chamber, the conical cover top is the most favorable force exerting component.

1. Spherical top cover with an opening in the center to sustain uniform pressure. The simplified mechanical model of the structure is shown in Figure 2-1. The internal boundary is connected to the rigid flange. The external boundary is considered as the solid support. When the limiting condition is reached, let us assume that the distortion velocity is

$$W = - A(\cos \varphi_0 - \cos \varphi)$$

(2-1)

As for the direction of W , the outer normal direction is positive.

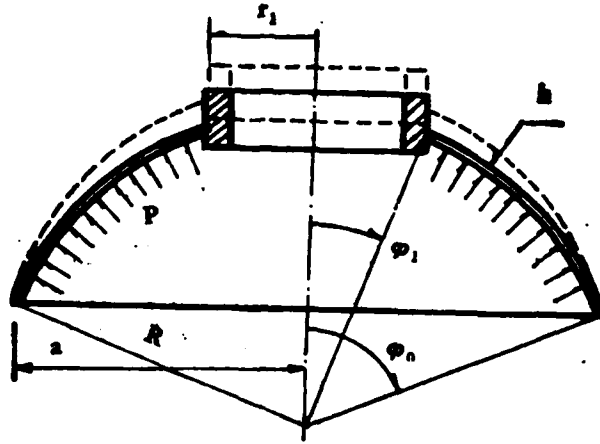


Figure 2-1

Using the mobile method and the jacketed shell yield condition, we can get, when $\varphi^* > \varphi_1$.

$$n = \frac{\sin^2 \varphi_0}{3K} \frac{(1-K)(\sin^2 \varphi^* - \sin^2 \varphi_1) + 2K \sin^2 \varphi_0 + 2(\cos \varphi^* - \cos \varphi_1) \cos \varphi_0}{(\cos \varphi_1 - \cos \varphi_0)(\cos \varphi_1 - \cos \varphi_0 + \sin^2 \varphi_1)} \quad (2-2)$$

when $\varphi^* < \varphi_1$.

$$n = \frac{2 \sin^2 \varphi_0}{3(\cos \varphi_1 - \cos \varphi_0)(\cos \varphi_1 - \cos \varphi_0 + \sin^2 \varphi_1)} \quad (2-3)$$

where

$$\varphi^* = \cos^{-1} \left(\frac{\cos \varphi_0}{1-K} \right) \quad (2-4)$$

$$K = \frac{h}{4R} \quad (2-5)$$

$$n = \frac{2}{3} \frac{PR^2 \sin^2 \varphi_0}{\sigma_s h^2} \quad (2-6)$$

The numerical results obtained from equations (2-2) and (2-3) are tabulated in Table 2-1.

The limiting loading capability curves are plotted as shown in Figure 2-2.

TABLE 2-1. The limiting loading capability of an opened spherical shell with external boundary solid support.

$\varphi_0 \backslash \varphi_1$	$\varphi_1=0^\circ$			$\varphi_1=10^\circ$			$\varphi_1=20^\circ$		
	$K=0.01$	0.02	0.05	0.01	0.02	0.05	0.01	0.02	0.05
10°	2.961								
20°	5.171	3.389	2.540	4.150	3.112	2.099			
30°	9.605	5.429	3.007	8.008	4.758	2.837	5.338	3.918	3.040
40°	14.780	7.975	3.873	13.210	7.238	3.622	9.643	5.255	3.176
50°	20.420	10.700	4.851	19.390	10.220	4.702	15.130	8.149	3.967
60°	25.750	13.250	6.765	24.340	13.550	5.505	20.630	10.750	4.851

Onat and Prager [1] gave the computation formula for the limiting loading capability of a spherical shell without opening in the presence of external boundary solid support, which corresponds to the $\varphi_1=0$ situation in this paper:

$$n = 2 + \frac{2}{(1 - \cos \varphi_0)^2 (1 - 2K)} \left[K(1 - 2K)^2 \sin^2 \varphi_0 + K^2 (1 - 2K - 4 \cos \varphi_0) \cos \varphi_0 \right. \\ \left. + (3K - 1) - \frac{1}{2K} (1 - 2K)^2 \ln(1 - 2K) \right] \quad (2-7)$$

where

$$n = \frac{PR}{\sigma_0 h}, K = \frac{h}{4R}$$

Li Kangxing, et al. gave an even more convenient formula [2]

$$n = 2 \left(1 + K \frac{1 + \cos \varphi_0}{1 - \cos \varphi_0} \right) \quad (2-8)$$

In order to compare the reliability of the results in this paper, a special case $\varphi_1=0$ within the range of applicable conditions is compared to (2-7) and (2-8). The numerical results are shown in Table 2-2 (equation (2-2) is written in a dimensionless form as (2-7)).

If the external boundary is considered as the simple support and the internal boundary is free, then by using an identical method, we can find that when $\varphi_0 > \varphi$

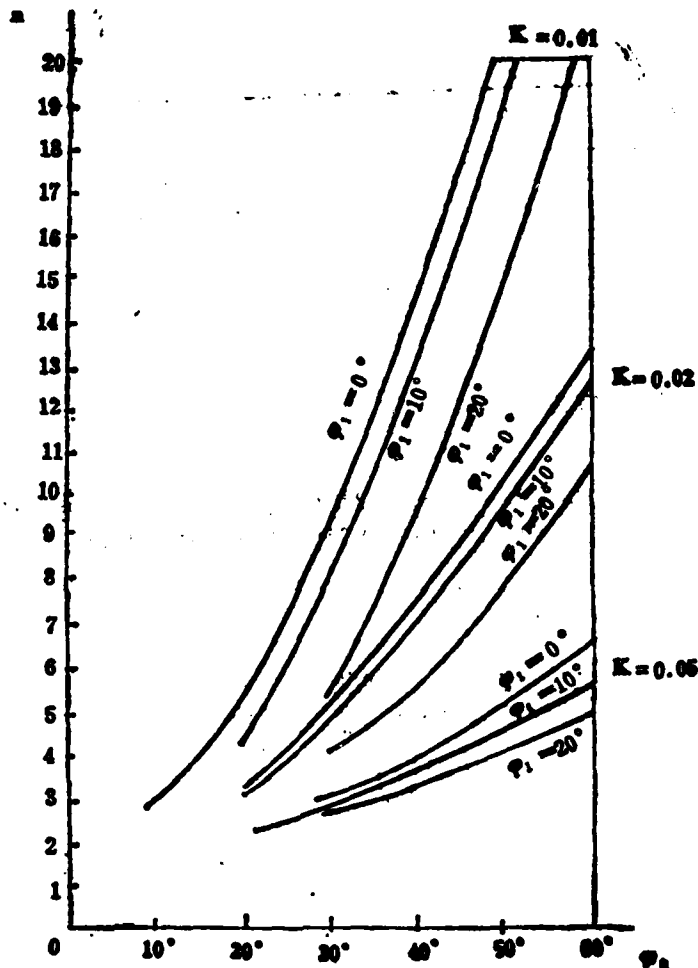


Figure 2-2

$$n = \frac{\sin^2 \varphi_0}{3K} \frac{(1-K) \sin^2 \varphi^* - \sin^2 \varphi_1 + K \sin^2 \varphi_0 + 2(\cos \varphi^* - \cos \varphi_1) \cos \varphi_0}{(\cos \varphi_1 - \cos \varphi_0)(\cos \varphi_1 - \cos \varphi_0 + \sin^2 \varphi_1)} \quad (2-9)$$

when $\varphi^* < \varphi_1$

$$n = \frac{\cos^2 \varphi_0}{3} \frac{\sin^2 \varphi_0 - \sin^2 \varphi_1}{(\cos \varphi_1 - \cos \varphi_0)(\cos \varphi_1 - \cos \varphi_0 + \sin^2 \varphi_1)} \quad (2-10)$$

where φ^*, K and n are the same as in (2-4), (2-5) and (2-6).

Reference [3] studied the opened spherical top cover under the same boundary condition by using the "dual moment weak interaction" yield condition. However, its expression and applicable region are very complicated. A comparison of the results of this paper to those in [3] is shown in Figure 2-3.

TABLE 2-2

φ°	1/40			1/80			1/160		
	n			n			n		
	本文	(3-6)	(3-7)	本文	(3-6)	(3-7)	本文	(3-6)	(3-7)
10°		3.580		6.290	5.265		4.301	3.635	
20°	3.944	3.609		2.781	2.804		2.400	2.402	
30°	2.739	2.697		2.866	2.848		2.186	2.179	
40°	2.394	3.377	2.891	2.192	2.189	2.119	2.084	2.094	2.096
50°	2.235	2.216	2.231	2.119	2.108	2.110	2.058	2.054	2.058
60°	2.198	2.150	2.153	2.076	2.075	2.080	2.037	2.038	2.039
70°	2.115	2.102	2.108	2.051	2.051	2.059	2.025	2.026	2.030
80°	2.071	2.071	2.074	2.035	2.035	2.036	2.018	2.018	2.020
90°	2.050	2.051	2.060	2.025	2.025	2.028	2.012	2.012	2.016

1--formula; 2--this paper; 3--this paper; 4--this paper

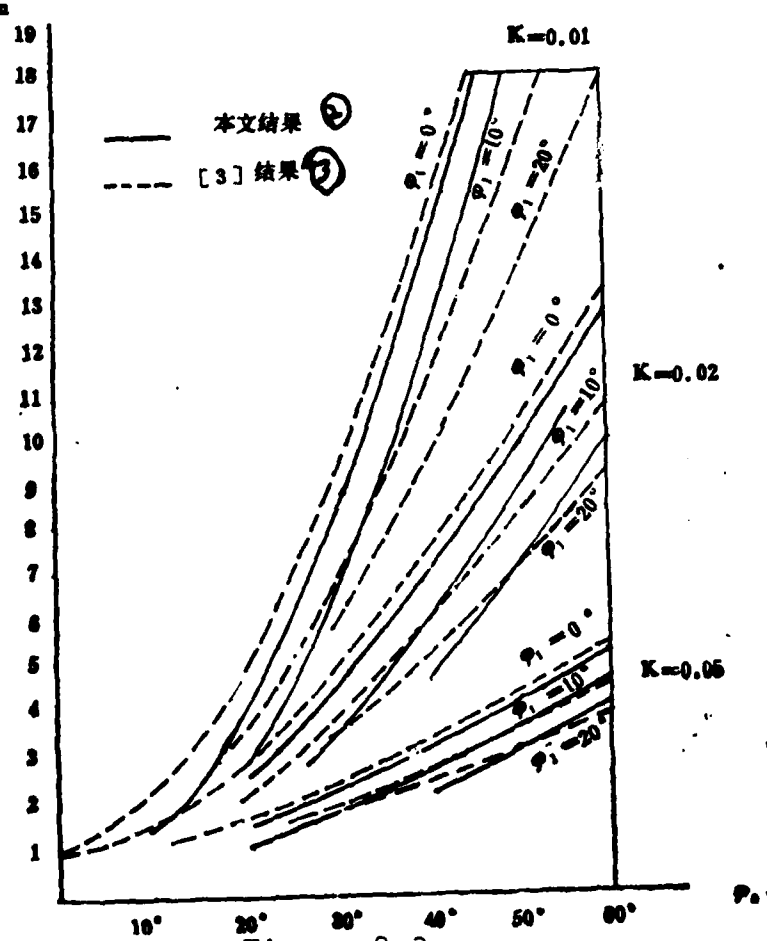


Figure 2-3

2--result of this paper; 3--result of [3]

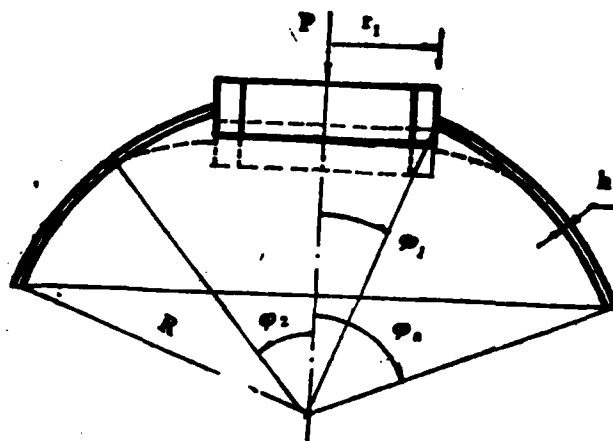


Figure 2-4

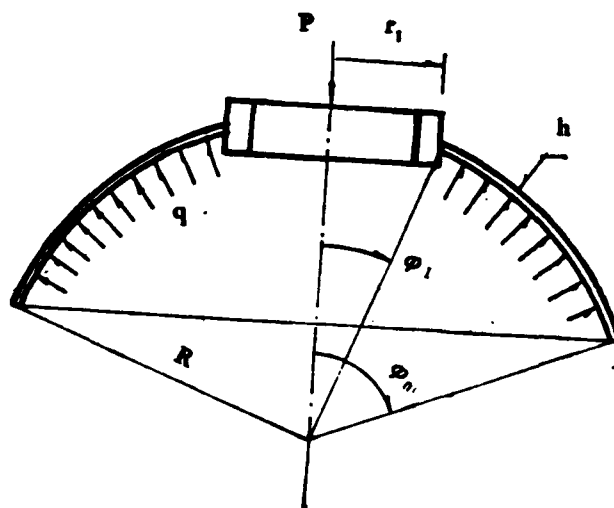


Figure 2-5

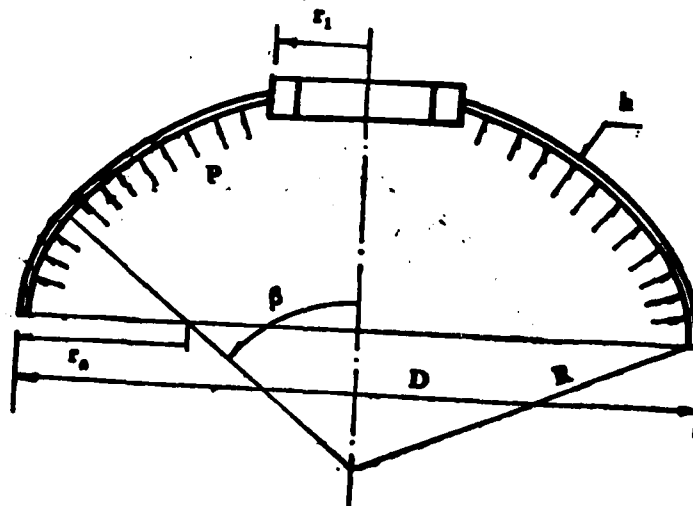


Figure 2-6

2. Spherical cover top with a center opening to sustain axially concentrated load. The mechanical model of the structure is shown in Figure 2-4. When reaching the limiting state, let us assume that the distortion speed is

$$W = A(\cos \varphi_1 - \cos \varphi_2) \quad (2-11)$$

where φ_2 is the position of the plastic region which is to be determined.

Using the mobile method and the packed shell yield condition, we can get

$$n = \frac{2\pi \left[2K + (1-K) \cos^2 \varphi_1 - 2 \cos \varphi_1 \cos \varphi_2 + \frac{1-2K}{1-K} \cos^2 \varphi_2 \right]}{\cos \varphi_1 - \cos \varphi_2} \quad (2-12)$$

where

$$\cos \varphi_2 = \cos \varphi_1 - \left(\frac{2K}{1-2K} \right)^{\frac{1}{2}} \sin \varphi_1 \quad (2-13)$$

$$n = \frac{P}{\sigma_s R h} \quad (2-14)$$

$$K = \frac{h}{4R} \quad (2-15)$$

If we assume that the structure is primarily designed to sustain axially concentrated load and simultaneously to stand the uniformly distributed internal pressure q , the mechanical model of the structure is simplified as shown in Figure 2-5.

If we assume that the internal pressure does not change the distortion speed (2-11) under the limiting condition, we can obtain the following using the similar method:

$$n = \frac{2\pi \left[2K + (1-K) \cos^2 \varphi_1 - 2 \cos \varphi_1 \cos \varphi_2 + \frac{1-2K}{1-K} \cos^2 \varphi_2 \right]}{\cos \varphi_1 - \cos \varphi_2} \quad (2-16)$$

where

$$+ \pi Q \frac{(\cos \varphi_1 - \cos \varphi_2)^2 + (\cos \varphi_1 - \cos \varphi_2) \sin^2 \varphi_1}{\cos \varphi_1 - \cos \varphi_2}$$

$$\cos \varphi_2 = \cos \varphi_1 - (\cos^2 \varphi_1 + \eta)^{\frac{1}{2}} \quad (2-17)$$

$$Q = \frac{qR}{\sigma_s h} \quad (2-18)$$

$$n = \frac{P}{\sigma_s R h} \quad (2-19)$$

$$\eta = \frac{4K - (2-2K+Q) \cos^2 \varphi_1 - 2Q \sin^2 \varphi \cos \varphi_1}{Q + \frac{2(1-2K)}{1-K}} \quad (2-20)$$

TABLE 2-3

试件编号 ⑦	材料屈服应力 $\sigma_s=28$ 公斤 毫米 ² ⑧	R 毫米③	h 毫米④	r ₁ 毫米⑤	q 公斤/毫米⑥	极限轴压(吨)⑨		误差 %⑩
						试验⑧	计算⑨	
1	不锈钢⑪	478	6	78	0	15	15.4	2.6
2	不锈钢⑫	478	6	78	0.6	32.5	33.3	2.5
3	不锈钢⑬	478	6	78	0.6	32.0	33.3	4.0

1--specimen no.; 2--yield stress of the material $\sigma_s=28$ kg/mm²;
3,4,5--mm; 6--kg/mm²; 7--limiting axial pressure (ton); 8--
experimental; 9--calculated; 10--error; 11--stainless steel;
12--stainless steel; 13--stainless steel;

Equations (2-12) and (2-16) agree better with the simulated tests. The comparison of the experimental results to the theoretical computation is shown in Table 2-3.

3. The triple centered top cover with an opening in the center to sustain the uniformly distributed internal pressure. The triple centered top cover is made of part of a spherical shell and a ring shell which are smoothly connected together. The simplified mechanical model is shown in Figure 2-6.

Let us assume that the distortion velocity is:
for the ring shell part

$$W = A(1 - \sin \varphi) \quad (2-21)$$

for the spherical shell part

$$W = A(1 - \sin \varphi) + B(\sin \beta - \sin \varphi) \quad (2-22)$$

ϕ = the first order derivative at β .

From continuity, we get

$$B = \frac{R}{r_0} A \quad (2-23)$$

The results obtained finally are tabulated in Table 2-4.

where

$$\alpha_1 = \arcsin \frac{r_0}{r_0 + H}$$

TABLE 2-4. The computation formula of limiting load capability of a triple centered top cover with a large opening under uniform pressure

公式 项	边界条件	内部于受约束, 外部固定或铰接 ⑤	内部铰接, 外部固定或铰接 ⑥
塑性铰变形功率 ⑦		$T' = \frac{r_0}{2r_0} \sigma_s b^2 \sin 2\varphi$	$T' = 0$
环壳部分变形功率 ⑧		$T_{II} = 2\sigma_s b' A R_0 \left[\left(1 - \frac{r_0}{R_0}\right) \left(\frac{\alpha}{2} + \alpha_0 - 2\beta\right) - \left(1 - \frac{r_0 + H}{2R_0}\right) \left(\frac{H}{2} - \alpha_0\right) + \left(\frac{4r_0}{R_0} - 1\right) \cos \beta - \left(\frac{2r_0}{R_0} - \frac{H}{r_0} - 1\right) \cos \alpha_0 \right. \\ \left. + \left(1 + \frac{H}{r_0} - \frac{r_0}{R_0}\right) \cos \alpha_0 + \frac{1}{2} \left(\frac{r_0 + H}{R_0}\right) \left(\sin 2\alpha_0 + \frac{1}{2} \sin 2\alpha_0\right) - \frac{r_0}{2R_0} \sin 2\beta \right]$	
球壳部分变形功率 ⑨		$T_{III} = 2\sigma_s b' A \frac{R}{r_0} \left[2\sigma (\cos \varphi_1 - \cos \beta) + \frac{1}{2} (R + H)(\sin 2\beta - \sin 2\varphi_1) + R(\varphi_1 - \beta) \right]$	
	$\varphi_1 < \varphi_2$	$T_{III} = 2\sigma_s b' A \frac{R}{r_0} \left[\sigma (3\cos \varphi_1 - \cos \varphi_2 + \cos \varphi_3 - 2\cos \beta) + R(\varphi_1 - \beta) + \frac{1}{2} (R + H)(\varphi_1 - \varphi_2) + \frac{1}{2} (R - H)(2\sin 2\beta - \sin 2\varphi_1 - 2\sin 2\varphi_2 + \sin 2\varphi_3) \right]$	
	$\varphi_1 < \varphi_2 < \varphi_3$	$T_{III} = 2\sigma_s b' A \frac{R}{r_0} \left[\sigma (\cos \varphi_1 - 2\cos \beta + \cos \varphi_3) + \frac{1}{2} (R + H)\varphi_1 + \frac{1}{2} (R - H)\varphi_2 - R\beta + \frac{1}{2} (R - H)(2\sin 2\beta - \sin 2\varphi_1 - \sin 2\varphi_2) \right]$	
	$\varphi_1 < \varphi_2 < \beta$	$T_{III} = 2\sigma_s b' A \frac{R}{r_0} \left[2\sigma (\cos \varphi_1 - \cos \beta) + R(\varphi_1 - \beta) + \frac{1}{2} (R - H)(\sin 2\beta - \sin 2\varphi_1) \right]$	
外力功 ⑩		$V = \sigma P A \left\{ \frac{R_0}{r_0} \left[2\sigma (\cos \varphi_1 - \cos \beta) + R(\varphi_1 - \beta) + \frac{1}{2} R (\sin 2\beta - \sin 2\varphi_1) + \frac{r_0^2}{2R_0} (\sigma - R \sin \alpha_0) \right] + 2r_0 \left[\left(R_0 - \frac{r_0}{2}\right) \times \left(\frac{\alpha}{2} - \beta\right) - (R_0 - r_0) \cos \beta - \frac{r_0}{4} \sin 2\beta \right] \right\}$	
最终表达式 ⑪		$V = T' + T_{II} + T_{III}$	

2--item; 3--formula; 4--boundary condition; 5--the internal strain is constrained, the external is fixed or hinged; 6--internally hinged and externally fixed or hinged; 7--plastic hinge distortion power; 8--distortion power of the ring shell part; 9--distortion power of the spherical shell part; 10--external force work; 11--final expression; 12--ring; 13--upper sphere; 14--lower sphere

TABLE 2-5. Table of numerical value of the load capability of a triple centered top cover with $r_1/D=0$

R/D	P/σ _s r ₀ /D	h/D 作者	0.010		0.016		0.020		0.026	
			文[4] ⑦	本文 ⑧	文[4] ⑤	本文 ⑥	文[4] ⑦	本文 ⑧	文[4] ④	本文 ⑩
1	0.15		0.0264	0.0286	0.0427	0.0426	0.0536	0.0534	0.0697	0.0696
1	0.25		0.0288	0.0309	0.0461	0.0495	0.0577	0.0620	0.0752	0.0808
1	0.30		0.0317	0.0330	0.0531	0.0529	0.0663	0.0662	0.0864	0.0862
1	0.35		0.0350	0.0350	0.0561	0.0561	0.0701	0.0701	0.0913	0.0913
1	0.40		0.0369	0.0369	0.0591	0.0590	0.0740	0.0738	0.0993	0.0991
0.8	0.20			0.0307		0.0493	0.0580	0.0617		0.0804

R/D	P/σ _s r ₀ /D	h/D 作者	0.030		0.034		0.040		0.046		0.050	
			文[4] ②	本文 ⑤	文[4] ③	本文 ④	文[4] ⑥	本文 ⑦	文[4] ⑧	本文 ⑨	文[4] ⑩	本文 ⑪
1	0.15		0.0806	0.0806	0.0916	0.0915	0.1082	0.1081	0.1249	0.1249	0.1359	0.1362
1	0.25		0.0869	0.0934	0.0987	0.1060	0.1105	0.1250	0.1343	0.1343	0.1464	0.1571
1	0.30		0.0998	0.0996	0.1132	0.1130	0.1335	0.1333	0.1538	0.1538	0.1675	0.1673
1	0.35		0.1053	0.1055	0.1186	0.1197	0.1410	0.1411	0.1624	0.1624	0.1768	0.1770
1	0.40		0.1112	0.1110	0.1261	0.1260	0.1486	0.1484	0.1712	0.1710	0.1863	0.1861
0.8	0.20		0.0988	0.0930		0.1055	0.1246	0.1245		0.1436	0.1565	0.1565

2--author; 3--reference [4]; 4--this paper; 5--reference [4];
 6--this paper; 7--reference [4]; 8--this paper; 9--reference [4];
 10--this paper; 11--author; 12--reference [4]; 13--this paper;
 14--reference [4]; 15--this paper; 16--reference [4]; 17--this paper;
 18--reference [4]; 19--this paper; 20--reference [4]; 21--this paper

$$\alpha_s = \arcsin \frac{-(R_0 + \frac{H}{U} - 2r_0) + \sqrt{(R_0 + \frac{H}{U} - 2r_0)^2 + 8(H+r_0)(R_0+H)}}{4(H+r_0)}$$

$$\varphi_s = \arcsin \frac{-a + \sqrt{a^2 + 4H(H-R)}}{2(H-R)}, \quad \varphi_r = \arcsin \frac{-a + \sqrt{a^2 + 2H(H-R)}}{2(H-R)}$$

$$h' = \frac{h}{2},$$

$$H = \frac{h}{4},$$

$$v = \frac{r_0}{R_0},$$

Reference [4] completed the load capability computation of a triple centered top cover without opening. The zero center opening angle is a special case in the applicable range of this paper. The comparison of this work and reference [4] is shown in Table 2-5.

The effects of various opening angles on the load capability of the triple centered top cover are shown in Tables 2-6 and 2-7.

TABLE 2-6. The effect of various opening angle on the load capability of the triple centered top cover

P/σ_c			h/D								
R/D	r_o/D	r_i/D	0.010	0.016	0.020	0.026	0.030	0.034	0.040	0.046	0.050
1	0.15	0	0.02657	0.04262	0.05338	0.06963	0.08055	0.09153	0.1081	0.1249	0.1362
1	0.15	0.10	0.02491	0.04007	0.05028	0.06576	0.07620	0.08675	0.1028	0.1190	0.1300
1	0.15	0.15	0.02328	0.03749	0.04711	0.06174	0.07163	0.08165	0.0969	0.1124	0.1230
1	0.15	0.20	0.02145	0.03467	0.04364	0.05733	0.06664	0.07608	0.0953	0.1053	0.1154
0.8	0.20	0.10	0.02828	0.04609	0.05778	0.07547	0.08737	0.09935	0.1175	0.1359	0.1482

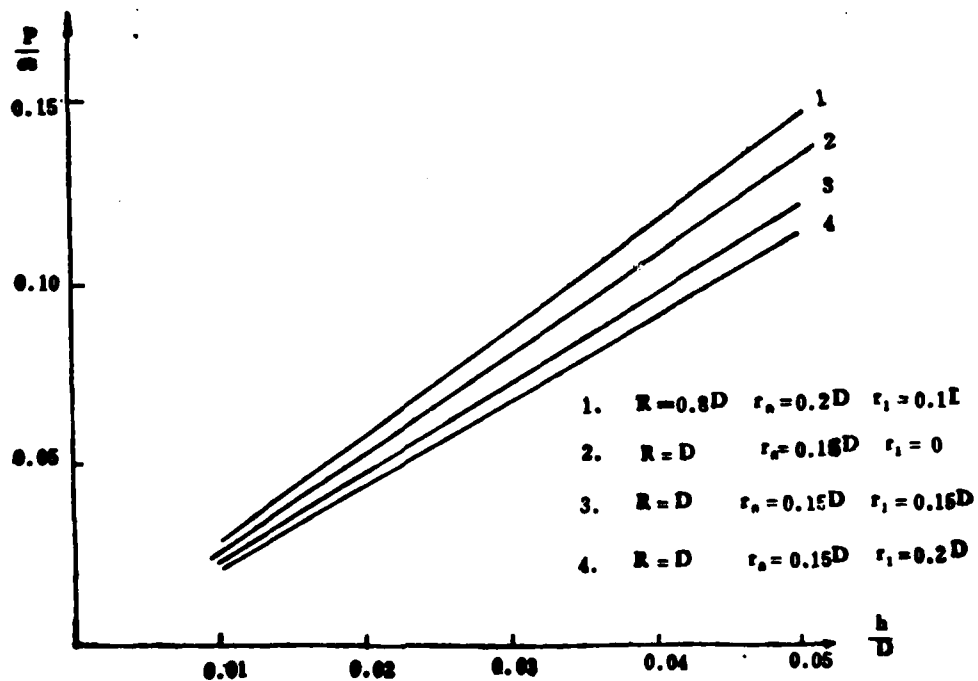


Figure 2-7

TABLE 2-7. Comparison of calculated and experimental results of load capabilities of a triple centered top cover sustaining uniform internal pressure

试件编号 ④	材料 $\sigma_s = 40$ 公斤/毫米 ² ⑤	$\frac{r_1}{D}$	$\frac{r_2}{D}$	$\frac{h}{D}$	$\frac{R}{D}$	承载能力试验值 P/σ_s ⑥	承载能力计算值 P/σ_s ⑦
1	不锈钢 ⑧	0.1055	0.1600	0.0082	0.9770	0.0200	0.0206
2	不锈钢 ⑧	0.1740	0.1600	0.0082	0.9770	0.0190	0.0194

4--specimen no.; 5--material $\sigma_s = 40 \text{ kg/mm}^2$; 6--load capability, experimental value; 7--load capability, calculated value; 8--stainless steel; 9--stainless steel

The computational formula given in this paper was proven to satisfactorily meet the engineering approximation requirement through experimental verification. The strain plate was used in the measurement of distortion. The theoretical computation can be simply obtained using an interpolation method from Table 2-6 and Figure 2-7. The experimental results are compared to the computed results and the comparison is shown in Table 2-7. The experimental results are given in Figures 2-8 and 2-9.

4. The limit analysis of the severed conical top cover sustaining concentrated load and the minimum weight design.

(1) Equal thickness severed conical shell. The simplified mechanical model is shown in Figure 2-10.

The limiting load capability is determined by the following formulas

$$P = \pi \sigma_s h \left[(x + r_2) \cos \alpha + \frac{h}{4} \sin^2 \alpha \right] + \frac{\pi}{2} \sigma_s h^2 \frac{X + r_2}{X - r_2} \sin^2 \alpha + \frac{1}{3} \pi q [x^2 + r_2(x + r_2)] \quad (2-24)$$

$$\frac{q}{\sigma_s h} x^2 + \frac{3}{2} \left(\cos \alpha - \frac{q r_2}{\sigma_s h} \right) x - (3 r_2 \cos \alpha) x + \frac{r_2^2}{2} \left[3(r_2 \cos \alpha - h \sin^2 \alpha) + \frac{q r_2^2}{\sigma_s h} \right] = 0 \quad (2-25)$$

The value of x determines the position of the plastic zone in the limiting state. It is represented by the distance from the shell surface to the rotational axis. From experiment and analysis, we

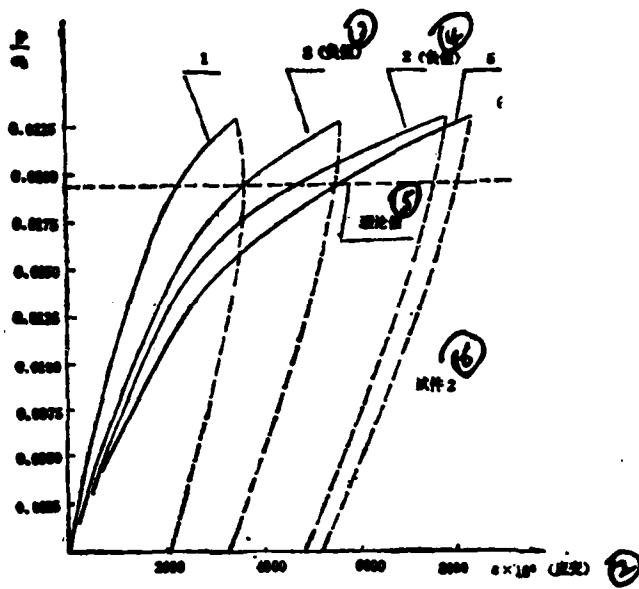


Figure 2-8

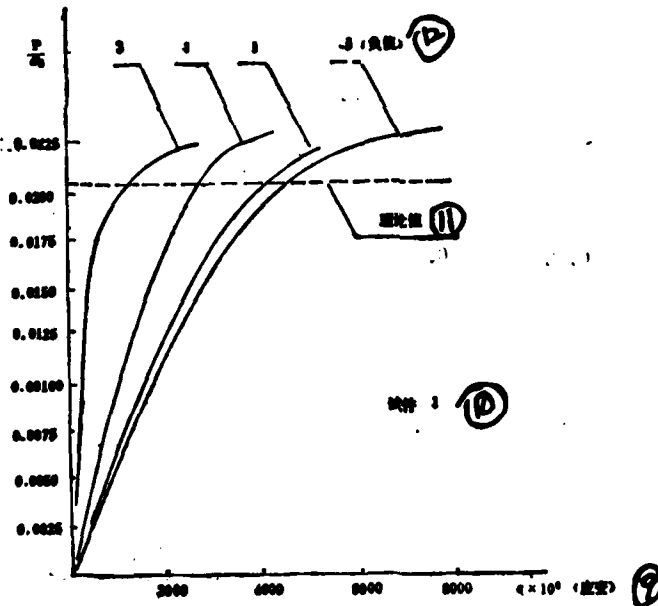


Figure 2-9

2--strain; 3--negative value; 4--negative value; 5--theoretical value; 6--specimen 2; 7--schematic diagram of the strain position; 9--strain; 10--specimen 1; 11--theoretical value; 12--negative value; 13--schematic diagram of the strain position

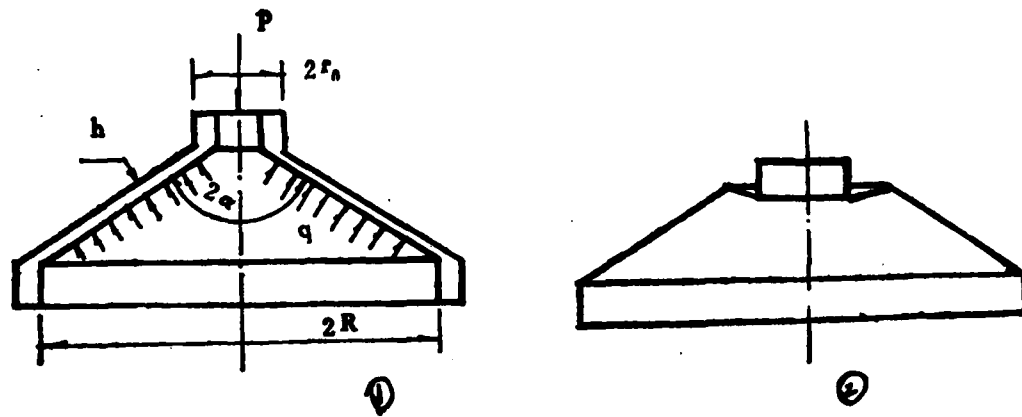


Figure 2-10
 1--equal thickness severed conical shell; 2--limiting status

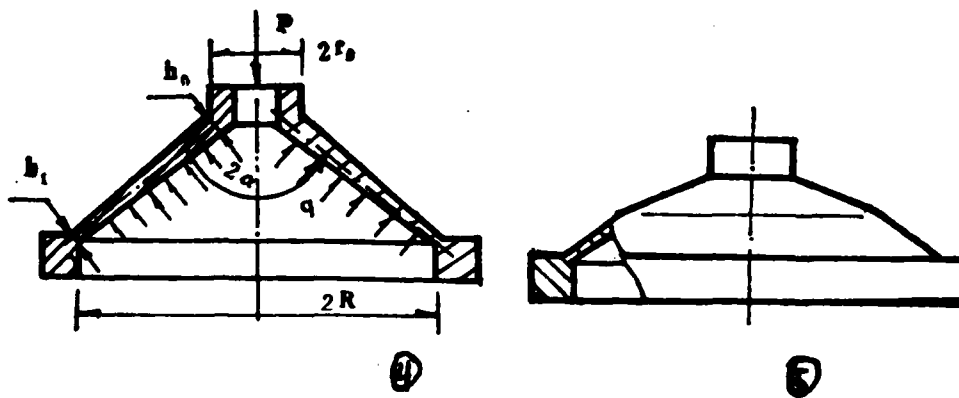


Figure 2-11
 4--linearly thickening severed conical shell; 5--limiting state

know that the destruction of the severed cone caused by the axially concentrated load only occurs in the local region in the small end. If the plastic zone can be extended toward the direction away from the small end, the loading capability can be improved. Let us consider such a conical shell thickness variation rate (or radially ribbed structural parameters). The limiting state corresponds to the situation that the plastic zone occurs in the entire region between the two end planes of the severed cone. The material utilization rate of

this structure is the highest. It is called the ideal thickening severed conical shell.

(2) The minimum weight design of a severed conical shell sustaining axial load. The mechanical model of the linearly thickening severed conical shell is shown in Figure 2-11.

The ideal thickness variation rate equation is

$$\begin{aligned} & \frac{h_i^2 \sin^2 \alpha}{12(R-r_o)^2} (14R^2 - 36r_o R^2 + 30r_o^2 R - 8r_o^3) \lambda^2 + \left[\frac{r_o h_o - 4R h_o}{3(R-r_o)} \cos \alpha \right. \\ & \left. - 15h_i^2 \frac{\sin^2 \alpha}{12(R-r_o)} \right] \lambda + h_o \cos \alpha - \frac{r_o h_o^2 \sin^2 \alpha}{(R-r_o)^2} + \frac{1}{3} \frac{q}{\sigma_s} (2R+r_o) = 0 \end{aligned} \quad (2-26)$$

To satisfy equation (2-26), the load capability of the severed conical shell is

$$\begin{aligned} P = \pi \sigma_s \left\{ \left[a(R+r_o) + \frac{2}{3} b(R^2 + Rr_o + r_o^2) \right] \cos \alpha + (h_i^2 - h_o^2) \frac{\sin^2 \alpha}{12(R-r_o)b} \right\} \\ + \frac{\pi}{2} \sigma_s \sin \alpha \frac{R h_i^2 + r_o h_o^2}{R-r_o} + \frac{1}{3} \pi q [R^2 + r_o(R+r_o)] \end{aligned} \quad (2-27)$$

in (2-26)

$$\lambda = 1 - \frac{h_i}{h_o} \quad (2-28)$$

The mechanical model of a radially ribbed severed conical shell is shown in Figure 2-12.

The ideal reinforcing rib distribution should satisfy the following parametric equation:

$$\begin{aligned} & \frac{2}{3} \left(\frac{n \delta H}{R r_o} + \frac{q}{\sigma_s} \right) R^2 - \left[\pi h + \frac{n \delta H}{2 R r_o} (R + 3 r_o) + \frac{q}{\sigma_s} r_o \right] R^2 \\ & + 2 \left(\pi h + \frac{n \delta H}{2} \frac{R + r_o}{R r_o} \right) R r_o - \frac{n \delta H r_o}{6 R} (3 R + r_o) - \pi h r_o^2 + [\pi h^2 r_o + n \delta H \\ & \times (H + h)] \frac{\sin^2 \alpha}{\cos \alpha} + \frac{1}{3} \frac{q}{\sigma_s} r_o^2 = 0 \end{aligned} \quad (2-29)$$

TABLE 2-8

试件 编号	截锥 性质	材料	σ_s 公斤/ 毫米 ²	α°	r_s 毫米	R 毫米	h 毫米	h_0 毫米	h_1 毫米	"	δ 毫米	H 毫米	q 公斤/ 毫米 ²	试验值 吨	理论值 吨
1	等厚	25#钢	22.8	65	27	104	4							11	10.7
2	等厚	25#钢	22.8	65	27	104	4							11	10.7
3	变厚	25#钢	22.8	65	27.8	104		8	4.6					22	23
4	变厚	不锈钢	20	62	62.5	140		8	4.9					67	56.6
5	变厚	不锈钢	20	62	62.5	140		12	7.9					90	90.6
6	变厚	不锈钢	20	60	25	90		6	2.8					16	16
7	等厚	25#钢	22.8	65	27	104	4					0.4	12	12.2	
8	加肋	25#钢	22.8	65	27	104	4			6	4	12		21	20.2
9	加肋	25#钢	22.8	65	27	104	4			10	4	12		25	24
10	加肋	25#钢	22.8	65	75	278	12			8	12	30		140	150
11	加肋	25#钢	22.8	65	27	104	4			6	4	12	0.2	19	20.3
12	加肋	25#钢	22.8	65	27	104	4			6	4	12	0.4	22	22
13	加肋	25#钢	22.8	65	27	104	4			6	4	12	0.6	23	24

2--specimen no.; 3--property of the severed cone; 4--material; 5-- σ_s kg/mm²; 6,7,8,9,10, 11,12--mm; 13--q kg/mm²; 14--experimental value, ton; 15--theoretical value, ton; 16--equal thickness; 17--equal thickness; 18--variable thickness; 19--variable thickness; 20--variable thickness; 21--variable thickness; 22--equal thickness; 23--ribbed; 24--ribbed; 25--ribbed; 26--ribbed; 27--ribbed; 28--ribbed; 29--25# steel; 30--25# steel; 31--25# steel; 32--stainless steel; 33--stainless steel; 34--stainless steel; 35--25# steel; 36--25# steel; 37--25# steel; 38--25# steel 39--25# steel; 40--25# steel; 41--25# steel

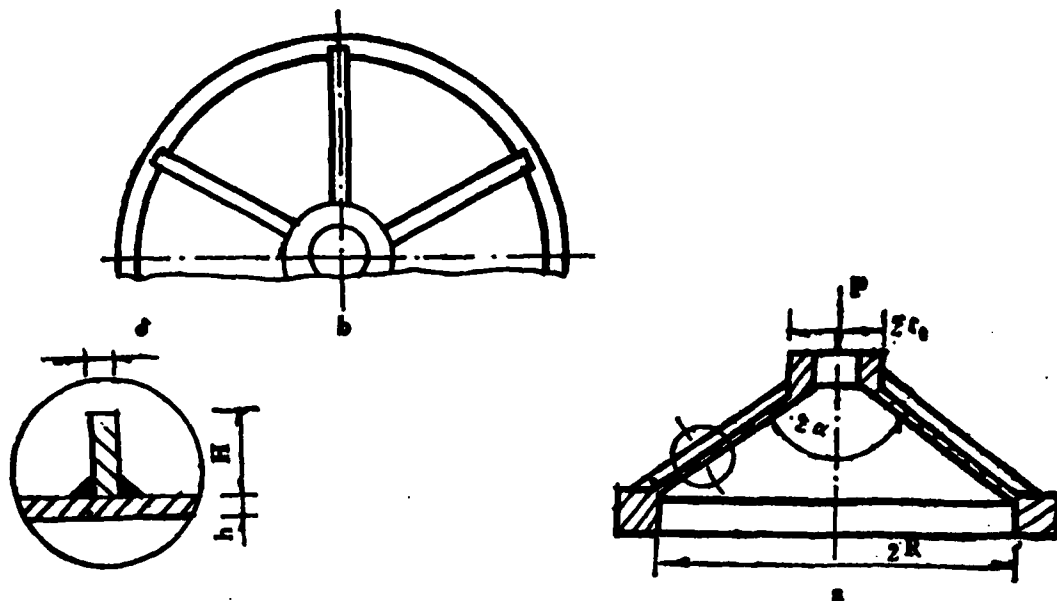


Figure 2-12

To satisfy (2-29), the structural load capability is

$$P = \pi \sigma_s \left\{ \left[a(R+r_o) + \frac{2}{3} b(R^2 + Rr_o + r_o^2) \right] \cos \alpha + \frac{h^2 \sin^2 \alpha}{4} \right\} + \frac{\sigma_s \sin^2 \alpha}{R-r_o} \left[\frac{\pi h^2}{2} (R+r_o) \right. \\ \left. + n \delta H (H+h) - \frac{n^2 \delta^2 H^2}{8\pi} \left(\frac{1}{R} + \frac{1}{r_o} \right) + \frac{\pi}{3} q [R^2 + r_o(R+r_o)] \right] \quad (2-30)$$

where n is the number of ribs, H is the height of the rib, δ is the thickness of the rib.

$$a = h + \frac{n \delta H}{2\pi} \frac{R+r_o}{Rr_o}$$

$$b = - \frac{n \delta H}{2\pi R r_o}$$

The reliability of the above analysis can be verified by simulation tests. The comparison of the experiment and the theoretical analysis is shown in Table 2-8.

III. THE LOAD CAPABILITY OF A CENTRIFUGAL TYPE INJECTOR DISK

The centrifugal injector disk is a complicated two layer circular plate structure. Its double layered wall divides the thrust chamber

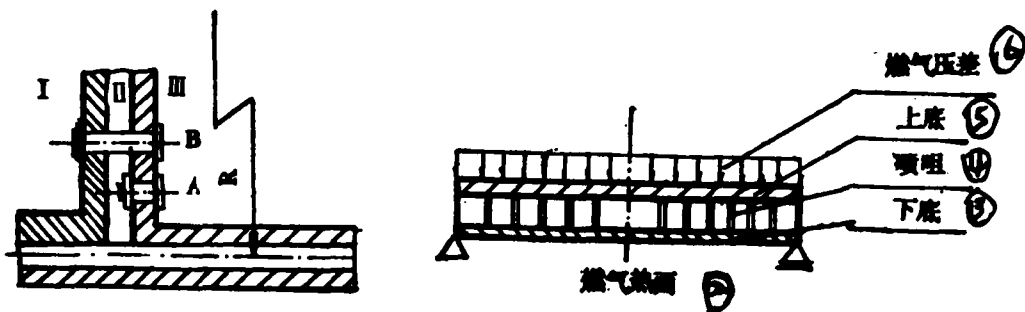


Figure 3-1a

2--combustion gas hot surface; 3--bottom; 4--nozzle; 5--top;
6--combustion gas pressure difference

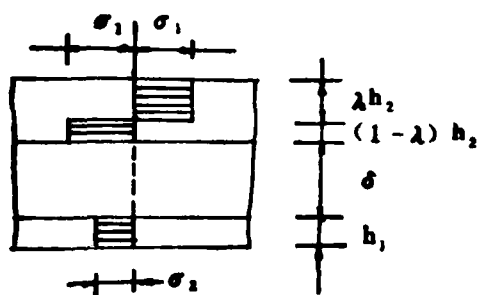
into the combustion chamber (see I and II in Figure 3-1), and the oxidant chamber (II or I) and the combustible gas chamber (III). The two layer plate was welded together. Generally speaking, the pressures P_1 and P_2 excited on I and II are approximately equal to and higher than P_{III} . Therefore, the injector disk of the entire unit only has to sustain the pressure drop $P_I - P_{III}$.

The mechanical model of the injector disk is shown in Figure 4-16. In the computation, the following basic assumptions are adopted [5]:

(1) The double layer circular plates were connected rigidly by many nozzles. There is no relative distortion. It is also considered that the nozzles are uniformly distributed on the plate.

(2) The bottom of the injector plate is working at high temperature. The temperature varies nonlinearly along the radial flow radius of the circular plate. The temperature is lowest near the edge of the circular plate. The temperature is the highest at the center of the circular plate. Let us assume that the temperature variation is

$$T(r) = T_0 - (T_0 - T_1)\rho^2 \quad (3-1)$$



where T_0 is the temperature at the center of the plate and T_k is the temperature at the edge of the plate. $\rho = \frac{r}{R}$; n is a constant greater than 1. r is the radial flow radius.

Figure 3-2

The limiting structural analysis assumed that thermal stress did not affect the limiting load capability. The temperature only affects the yield stress value of the material.

If the temperature difference between the center and edge of the circular plate is not too large, the difference in the value of the material yield stress can be obtained using a linear difference method. Therefore, we can write the following linear relation:

$$\sigma_s(T) = \sigma_s(1 - KT) \quad (3-2)$$

where σ_s -- yield stress at constant temperature ($T=0$)

K -- a constant which varies with the material.

Consequently, we can obtain

$$\sigma_s(r) = \sigma_s(c + d\rho^n) \quad (3-3)$$

where

$$d = K(T_0 - T_k), \quad c = 1 - KT_0 \quad (3-4)$$

(3) The yielding bending moment of the double layer circular plate. Under the yield condition, the stress distribution along the height of the plate is as shown in Figure 4-2. Because $\sigma_s(T) = \sigma_s(c + d\rho^n)$, $\sigma_s = \text{constant}$.

Yielding bending moment

$$M_s(r) = M_s \left\{ 1 + 2a\beta(c + d\rho^n) \left[\gamma - \frac{1}{2}a\beta(c + d\rho^n) \right] \right\} \quad (3-5)$$

where

$$M_s = \frac{\sigma_s h_1^2}{4}$$

$$\gamma = 1 + a + \frac{2\delta}{h_1},$$

$$a = \frac{h_1}{h_2},$$

$$\beta = \frac{\sigma_1}{\sigma_s}$$

(4) The effect of the nozzles. A series of densely located nozzles would weaken the load capability of the circular plate. Reference [5] suggested that this effect be included in the internal power of the corresponding velocity field. This is a very complicated method. However, [6] recommended the use of a functional coefficient to take this effect into account:

$$\xi = 1 - \frac{F_0}{F} \quad (3-6)$$

F_0 -- the area of the opening of the nozzles to the plate.

F -- the total area of the plate.

The injector disk is formed by two layers of plates. On top of the double layer plate, the apertures of the nozzle are not equal. The effect coefficient should be correspondingly noted as

$$\xi_1 = 1 - \frac{F_{01}}{F_1} \quad (3-7)$$

$$\xi_2 = 1 - \frac{F_{02}}{F_2}$$

Therefore, the opening of holes on the nozzle to the circular plate is considered:

$$\begin{aligned} \sigma_1(T) &= \sigma_1(c + d\rho^n)\xi_1 \\ \sigma_2 &= \sigma_1 \cdot \xi_2 \end{aligned}$$

On the aforementioned basis, if the edge support of the injector disk is considered as a simple support, the load capability sustaining uniformly distributed pressure is:

$$P = \frac{6M_1}{R^2} \left\{ 1 + 2\alpha\beta\gamma \left(c + \frac{d}{n+1} \right) - \alpha^2\beta^2 \left(c^2 + \frac{2cd}{n+1} + \frac{d^2}{2n+1} \right) \right\} \quad (3-8)$$

where the symbols are the same as in (3-5), and $\beta = \frac{\sigma_1}{\sigma_2} \cdot \frac{\xi_1}{\xi_2}$.

If the edge support of the injector disk is considered as a fixed support, then

$$P = \frac{6M_1}{R^2\rho_b^2} \left[1 + 2\alpha\beta\gamma \left(c + \frac{d\rho_b}{n+1} \right) - \alpha^2\beta^2 \left(c^2 + \frac{2cd\rho_b}{n+1} + \frac{d^2\rho_b^2}{2n+1} \right) \right] \quad (3-9)$$

where ρ_b is determined by the following formula:

$$A\rho_b^{2(n+1)} + B\rho_b^{2n} + G\rho_b^{2n-2} - D\rho_b^2 + E\rho_b \ln \rho_b + K\rho_b - L = 0 \quad (3-10)$$

$$A = \frac{\alpha^2 \beta^2 d^2 (1-n)}{2(2n+1)}$$

$$B = \frac{3\alpha^2 \beta^2 d^2}{2(2n+1)}$$

$$G = \frac{\alpha \beta d (\gamma - \alpha \beta c) (n-2)}{n(n+1)}$$

$$D = \frac{3\alpha \beta d (\gamma - \alpha \beta c)}{n+1}$$

83

$$E = \alpha \beta c (\alpha \beta c - 2\gamma) - 1$$

$$K = \frac{\alpha \beta d}{n} \left[2(\gamma - d\beta c) - \frac{1}{2} \alpha \beta d \right] + \frac{5}{2} + \alpha \beta \left[\gamma(5c + 2d) - \alpha \beta \left(\frac{5}{2} c^2 + 2dc + d^2 \right) \right]$$

84

$$L = \frac{3}{2} [1 + \alpha \beta c (2\gamma - \alpha \beta c)]$$

IV. THE LOAD CAPABILITY OF THE COMBUSTION CHAMBER

The load capability of the combustion chamber is the load capability of the combustion chamber itself. The weak part of the chamber is in the cylindrical section. It is the representative section for checking the strength.

The cylindrical section has densely located reinforced ribs along the circumferential direction. The inner and outer walls are connected by wavy boards longitudinally. Obviously, this is a dual directional jacketed cylindrical shell with reinforced ribs. It can sustain the combined effect of the uniform internal pressure and the axial force. Assuming that the cylindrical shell is supported rigidly on both sides, let us also assume that:

(1) a high pressure coolant is passed between the inner and outer walls. It is considered not to be related to the load capability.

(2) The inner wall temperature of the combustion chamber is the average value along the axial and wall thickness directions, i.e.,

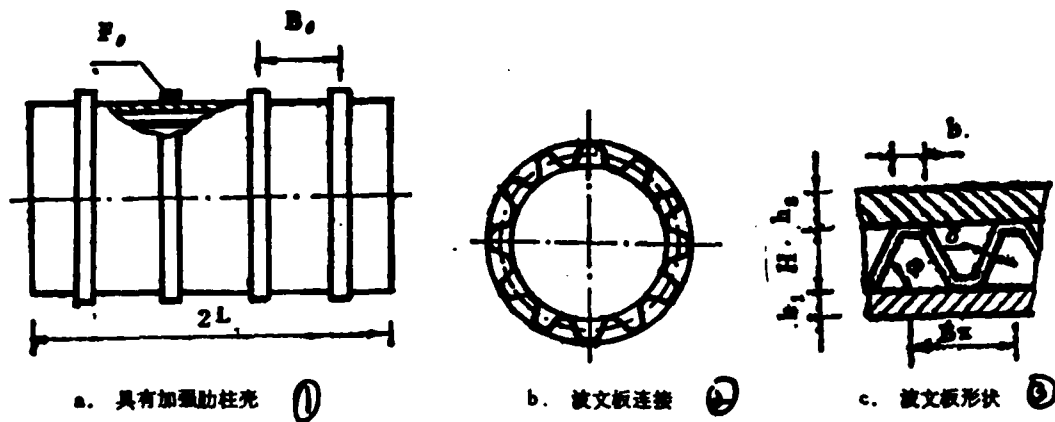


Figure 4-1

1--with reinforced ribs; 2--connected by wavy board; 3--shape of the wavy board

the inner wall yield stress is a constant. Because the inner wall is thinner, and the work is done at high temperatures, the material property is low. It does not contribute greatly to the load capability. Therefore, this type of simplification will not bring about large effects.

The mechanical model of the simplified cylindrical section of the combustion chamber is shown in Figure 4-1.

Based on the above assumptions, using the force method and the simplified yield condition, we can get the load capability

$$n = 1 + a_\theta + \frac{4 - 2\phi - 2\phi a_\theta + 4a_x}{2\phi + c^2(1 + a_x)^2} \quad (4-1)$$

where

a_θ , a_x are the relevant dimensionless parameters with respect to circumferential reinforced ribs and axial reinforced ribs, respectively;

ϕ is the axial force coefficient, which reflects the cylindrical shell characteristics of the half opening of the combustion chamber

c^2 is the structural parameter of the cylindrical shell

n is the limiting value of the dimensionless uniform pressure.

They are equal to the following, respectively:

$$a_1 = \frac{F_x \sigma_{30}}{B_x (\sigma_1 h_1 + \sigma_2 h_2)}, \quad a_2 = \frac{F_x \sigma_{30}}{B_x (\sigma_1 h_1 + \sigma_2 h_2)}$$

$$\varphi = 1 - \frac{R}{\pi R^2 P}, \quad c^2 = \frac{L^2}{R} \frac{\sigma_1 h_1 + \sigma_2 h_2}{M_x^S}$$

$$n = \frac{PR}{\sigma_1 h_1 + \sigma_2 h_2}$$

h_1, h_2 are the thickness of the inner and outer wall respectively

R is the average radius of the cylindrical section of the combustion chamber

\bar{R} is the thrust of the engine

P is the combustible gas pressure in the cylindrical section of the combustion chamber

σ_1, σ_2 are the material yield stresses corresponding to the inner and outer walls at average temperature

L is half the length of the cylindrical section of the combustion chamber

B_x is the wave distance of the wavy board

B_o is the spacing between the reinforced ribs in the circumferential direction

σ_{30} is the material yield stress of the reinforced rib in the circumferential direction

F_x is the cross-sectional area of the wavy board within a wave length

F_θ is the cross-sectional area of a reinforced rib in the circumferential direction

M_x^S is the yielding variable moment on a unit length of the jacketed layer formed by the inner and outer walls, including the wavy board.

$$M_x^S = \frac{\sigma_1 h_1^2}{4} \left[1 + 2 \frac{\sigma_1}{\sigma_2} \frac{h_1}{h_2} \left(1 + \frac{h_1}{h_2} - \frac{1}{2} \frac{\sigma_1}{\sigma_2} \frac{h_1}{h_2} + 2 \frac{H}{h_2} \right) + 2 \frac{\sigma_{30}}{\sigma_1} \frac{F_x}{B_x h_1} \left(1 - \frac{\sigma_1}{\sigma_2} \frac{h_1}{h_2} - \frac{1}{2} \frac{\sigma_{30}}{\sigma_2} \frac{F_x}{B_x h_2} + \frac{H}{h_1} \right) \right]$$

H is the height of the wavy board, which is also the distance between the inner and outer walls.

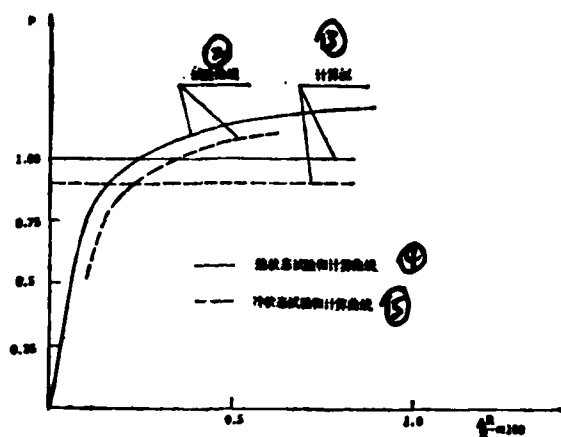


Figure 4-2. The load capability of a ribless combustion chamber
 2--experimental curve; 3--calculated value; 4--hot state experiment and calculated curves; 5--cold state experimental and calculated curves

σ_{3x} is the yield stress of the wavy board material

$$F_s = 2 \left(\frac{H}{\sin \varphi_s} + b \right) \delta,$$

where δ is the thickness of the wavy board.

Equation (4-1) agrees well with the experimental results. Figure 4-2 shows the comparison of the experimental curve and the theoretical computation of the load capability of a ribless combustion chamber.

V. THE LOAD CAPABILITY OF TUBE BUNDLE NOZZLES

The simplified mechanical model of the tube bundle nozzles is shown in Figure 5-1. The exerted combustible gas pressure is assumed to be

$$P = P_0 e^{-\lambda x} \quad (5-1)$$

Solving the set of equations:

$$\begin{cases} f_1(\varphi_1) + f_2(\varphi_1)P_0 + f_3(\varphi_1)c = 0 \\ f_1(\varphi_2) + f_2(\varphi_2)P_0 + f_3(\varphi_2)c = 0 \\ g_1(\varphi_1) + g_2(\varphi_1)P_0 + g_3(\varphi_1)c = 0 \\ g_1(\varphi_2) + g_2(\varphi_2)P_0 + g_3(\varphi_2)c = 0 \end{cases}$$

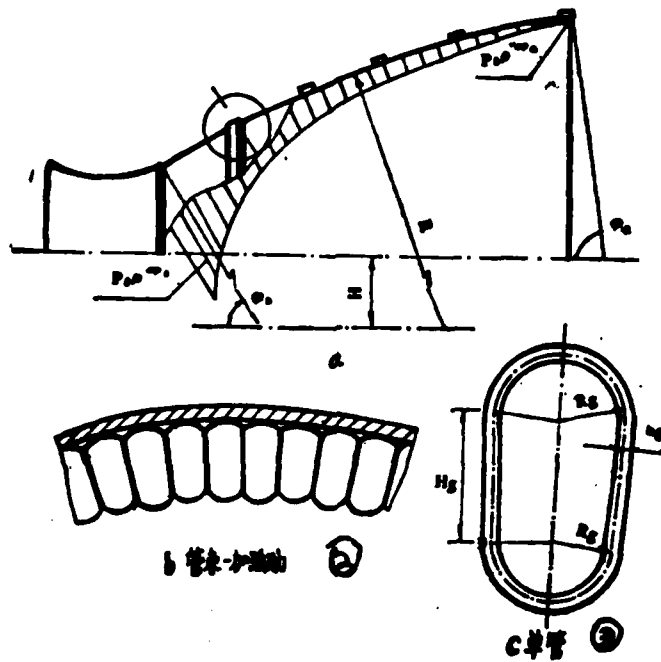


Figure 5-1
2--tube bundles--reinforced rib; 3--single tube

where the functions are as follows:

$$\left\{ \begin{aligned} f_1(\varphi) &= A_1 \cos \varphi + RN^2(\varphi \cos \varphi - \sin \varphi) + M_s \frac{R \sin \varphi - H}{R} \\ f_2(\varphi) &= A_1 \cos \varphi + RN^2(\varphi \cos \varphi - \sin \varphi) - M_s \frac{R \sin \varphi - H}{R} \\ f_3(\varphi) &= A_2 \cos \varphi + A_3 \sin \varphi - \left[\frac{RH}{1+a^2} - \frac{R^2(2 \cos \varphi + a \sin \varphi)}{a^2 + 4a} \right] e^{-a\varphi} \end{aligned} \right.$$

$$\left\{ \begin{aligned} f_4(\varphi) &= A_4 \cos \varphi + \frac{1}{R} \\ g_1(\varphi) &= -A_1 \frac{R - H \sin \varphi}{R \sin \varphi - H} - N^2 \frac{R(R\varphi - R \sin \varphi \cos \varphi - H\varphi \sin \varphi)}{R \sin \varphi - H} \\ g_2(\varphi) &= \left\{ \frac{RH a}{1+a^2} + \frac{R^2 H \cos \varphi}{(1+a^2)(R \sin \varphi - H)} - \frac{R^2[(2+a^2) \sin \varphi + a \cos \varphi]}{a^2 + 4a} \right. \\ &\quad \left. - \frac{R^2 \cos \varphi (2 \cos \varphi + a \sin \varphi)}{(a^2 + 4a)(R \sin \varphi - H)} \right\} e^{-a\varphi} - A_1 \frac{R - H \sin \varphi}{R \sin \varphi - H} - A_4 \frac{H \cos \varphi}{R \sin \varphi - H} \\ g_3(\varphi) &= - \left(A_4 \frac{R - H \sin \varphi}{R \sin \varphi - H} + \frac{\cos \varphi}{R \sin \varphi - H} \right) \end{aligned} \right.$$

8

where the structural parameters and material characteristics parameters are

$$A_1 = \frac{R \sin \varphi_0 - H}{R \cos \varphi_0} M_0^z - R(\varphi_0 - \operatorname{tg} \varphi_0) N_0^z$$

$$A_2 = - \left[\frac{R^2(a \sin 2\varphi_0 + 2 \cos 2\varphi_0)}{2(a^2 + 4)} + \frac{RH(\sin \varphi_0 - a \cos \varphi_0)}{1 + a^2} \right] \operatorname{tg} \varphi_0 e^{-a\varphi_0}$$

$$- \left[\frac{R^2(2 + a \operatorname{tg} \varphi_0)}{a^2 + 4a} - \frac{RH}{(1 + a^2) \cos \varphi_0} \right] e^{-a\varphi_0}$$

$$A_3 = - \frac{1}{R \cos \varphi_0}$$

$$A_4 = \left[\frac{R^2(2 \sin 2\varphi_0 + 2 \cos 2\varphi_0)}{2(a^2 + 4)} + \frac{RH(\sin \varphi_0 - a \cos \varphi_0)}{1 + a^2} \right] e^{-a\varphi_0}$$

$$M_0^z = \frac{\sigma_0 h_0}{2R_0 + h_0} \left[\frac{1}{2} H_0^2 + \pi R_0 H_0 + 4R_0^2 \right]$$

$$N_0^z = \frac{\sigma_0 h_0^2}{R_0}$$

VI. THE LOCAL STRENGTH OF THE COMBUSTION CHAMBER

The so-called local strength is the uniform load resistance of the cooling conduit of the combustion chamber and the connection strength of the wavy board. Their characteristic is that the structural dimension is so small that it is extremely difficult to reasonably simplify the computational model. The computational formula given here, after experimental verification, has sufficient accuracy for the specific problem of the engine.

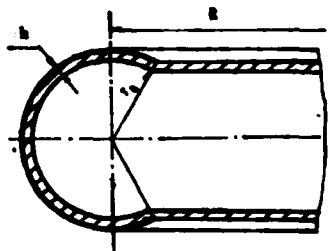
(1) The connection strength of the wavy board. The simplified mechanical model is shown in Figure 6-1. Let us take an element in the combustion chamber for analysis.

The drill weld strength is a statically determined problem. Equations (6-1) and (6-2) are the destructive strength, which is used to replace the load capability.

VII. THE RING SHAPED FLUID COLLECTING RING

The schematic diagram of the structure is shown in Figure 7-1.

The uniform pressure load capability [7] is:



$$\text{the upper limit solution } P_{\text{up}} = \frac{\sigma_s}{\beta} \frac{1 + \frac{1}{2}\pi a}{1 + \frac{1}{4}\pi a} \quad (7-1)$$

$$\text{Figure 7-1 the lower limit solution } P_{\text{down}} = \frac{\sigma_s}{\beta} \frac{1 + \sigma}{1 + \frac{1}{4}\pi a} \quad (7-2)$$

where

$$a = \frac{r_0}{R_0},$$

$$\beta = \frac{r_0}{h}$$

REFERENCES:

- [1] E. T. Onat, W. Prager. Limit analysis of shells of revolution. Proc. Roy. Netherlands Acad. Sci., B, 57, 1954, 534-548. Translated Book of Mechanics, Vol. 4, Shanghai Scientific Technical Translation Institute, 1963
- [2] Li Kangxing et al. "Load Capability Limit of Shells of Revolution", Shanghai Jiaotong University Research Institute Editing 1963.
- [3] P. G. Hodge, Jr., C. Lakshminathan: Yield Point Loads of Spherical Caps with Cutouts. Applied Mechanics, Vol. 11, 1962.
- [4] Li Kangxing et al. "The Load Capability Limit of Triple Centered Top Covers", Symp. of the 1st Limit Analysis and Plastic Theory Conf. of the Chinese Mechanics Society, 86-93.
- [5] L.I. Polyakov, M.A. Rudie. Some problems of limiting equilibrium of circular plates considering temperature effects. Thermal stresses in construction elements. Doklady Nauchnogo Soveshchaniya, No. IV, 1964, 233-240.

- [6] Fayordoyev: The Thermal Stress Part Strength of a Liquid Rocket Engine, Defense Industrial Publications, 1965, 112-210.
- [7] Yu. M. Listrova, M.A. Rudie. Limiting equilibrium of a toroidal shell. Izvestiya AN SSSR, OTN. Mekhaniki and Mashinostroyeniye, 1963, 3, 119-123.

DISTRIBUTION LIST

DISTRIBUTION DIRECT TO RECIPIENT

<u>ORGANIZATION</u>	<u>MICROFICHE</u>
A205 DMAHTC	1
A210 DMAAC	1
B344 DIA/RTS-2C	9
C043 USAMIIA	1
C500 TRADOC	1
C509 BALLISTIC RES LAB	1
C510 R&T LABS/AVRADCOM	1
C513 ARRADCOM	1
C535 AVRADCOM/TSARCOM	1
C539 TRASANA	1
C591 FSTC	4
C619 MIA REDSTONE	1
D008 NISC	1
E053 HQ USAF/INET	1
E403 AFSC/INA	1
E404 AEDC/DOF	1
E408 AFWL	1
E410 AD/IND	1
E429 SD/IND	1
P005 DOE/ISA/DDI	1
P050 CIA/OCR/ADD/SD	2
AFIT/LDE	1
FTD	
CCN	1
NIA/PHS	1
NIIS	2
LLNL/Code L-389	1
NASA/NST-44	1
NSA/1213/TDL	2

END

FILMED

6-83

DTIC